The Astronomical Journal, 168:202 (19pp), 2024 November https://doi.org/10.3847/1538-3881/ad6f07

TOI 762 A b and TIC 46432937 b: Two Giant Planets Transiting M-dwarf Stars

Joel D. Hartman[1], Daniel Bayliss[2,3], Rafael Brahm[4,5,6], Edward M. Bryant[7], Andrés Jordán[4,5,6], Gáspár Á. Bakos[1], Melissa J. Hobson[8], Elyar Sedaghati[9], Xavier Bonfils[10], Marion Cointepas[8,10], Jose Manuel Almenara[8,10], Khalid Barkaoui[11,12,13], Mathilde Timmermans[11], George Dransfield[14], Elsa Ducrot[15,28], Sebastián Zúñiga-Fernández[11], Matthew J. Hooton[16], Peter Pihlmann Pedersen[16], Francisco J. Pozuelos[17], Amaury H. M. J. Triaud[14], Michaël Gillon[11], Emmanuel Jehin[18], William C. Waalkes[19], Zachory K. Berta-Thompson[20], Steve B. Howell[21], Elise Furlan[22], George R. Ricker[23], Roland Vanderspek[23], Sara Seager[12,23,24], Joshua N. Winn[1], Jon M. Jenkins[21], David Rapetti[21,25], Karen A. Collins[26], David Charbonneau[26], Christopher J. Burke[23], and David R. Rodriguez[27]
[1] Department of Astrophysical Sciences, Princeton University, 4 Ivy Lane, Princeton, NJ 08544, USA; jhartman@astro.princeton.edu
[2] Department of Physics, University of Warwick, Gibbet Hill Road, Coventry, CV4 7AL, UK
[3] Centre for Exoplanets and Habitability, University of Warwick, Gibbet Hill Road, Coventry, CV4 7AL, UK
[4] Millennium Institute of Astrophysics (MAS), Nuncio Monseñor Sótero Sanz 100, Providencia, Santiago, Chile
[5] Facultad de Ingeniería y Ciencias, Universidad Adolfo Ibáñez, Av. Diagonal las Torres 2640, Peñalolén, Santiago, Chile
[6] Data Observatory Foundation, Santiago, Chile
[7] Mullard Space Science Laboratory, University College London, Holmbury St Mary, Dorking, RH5 6NT, UK
[8] Observatoire de Genève, Département d'Astronomie, Université de Genève, Chemin Pegasi 51b, 1290 Versoix, Switzerland
[9] European Southern Observatory (ESO), Av. Alonso de Córdova 3107, 763 0355 Vitacura, Santiago, Chile
[10] Univ. Grenoble Alpes, CNRS, IPAG, F-38000 Grenoble, France
[11] Astrobiology Research Unit, Université de Liège, Allée du 6 Août 19C, B-4000 Liège, Belgium
[12] Department of Earth, Atmospheric, and Planetary Sciences, Massachusetts Institute of Technology, 77 Massachusetts Avenue, Cambridge, MA 02139, USA
[13] Instituto de Astrofísica de Canarias (IAC), Calle Vía Láctea s/n, 38200, La Laguna, Tenerife, Spain
[14] School of Physics & Astronomy, University of Birmingham, Edgbaston, Birmingham, B15 2TT, UK
[15] AIM, CEA, CNRS, Université Paris-Saclay, Université de Paris, F-91191 Gif-sur-Yvette, France
[16] Cavendish Laboratory, University of Cambridge, JJ Thomson Avenue, Cambridge, CB3 0HE, UK
[17] Instituto de Astrofísica de Andalucía (IAA-CSIC), Glorieta de la Astronomía s/n, 18008 Granada, Spain
[18] Space Sciences, Technologies and Astrophysics Research (STAR) Institute, Université de Liège, Allée du 6 Août 19C, B-4000 Liège, Belgium
[19] Department of Physics and Astronomy, Dartmouth College, Hanover, NH 03755, USA
[20] Department of Astrophysical & Planetary Sciences, University of Colorado Boulder, Boulder, CO 80309, USA
[21] NASA Ames Research Center, Moffett Field, CA 94035, USA
[22] NASA Exoplanet Science Institute, Caltech/IPAC, Mail Code 100-22, 1200 E. California Blvd., Pasadena, CA 91125, USA
[23] Department of Physics and Kavli Institute for Astrophysics and Space Research, Massachusetts Institute of Technology, Cambridge, MA 02139, USA
[24] Department of Aeronautics and Astronautics, Massachusetts Institute of Technology, 77 Massachusetts Avenue, Cambridge, MA 02139, USA
[25] Research Institute for Advanced Computer Science, Universities Space Research Association, Washington, DC 20024, USA
[26] Center for Astrophysics | Harvard & Smithsonian, 60 Garden Street, Cambridge, MA 02138, USA
[27] Space Telescope Science Institute, 3700 San Martin Drive, Baltimore, MD 21218, USA
Received 2024 February 28; revised 2024 July 8; accepted 2024 July 9; published 2024 October 10

Abstract

We present the discovery of TOI 762 A b and TIC 46432937 b, two giant planets transiting M-dwarf stars. Transits of both systems were first detected from observations by the NASA TESS mission, and the transiting objects are confirmed as planets through high-precision radial velocity observations carried out with Very Large Telescope/ESPRESSO. TOI 762 A b is a warm sub-Saturn with a mass of $0.251 \pm 0.042\,M_{\rm J}$, a radius of $0.744 \pm 0.017\,R_{\rm J}$, and an orbital period of 3.4717 days. It transits a mid-M-dwarf star with a mass of $0.442 \pm 0.025\,M_{\odot}$ and a radius of $0.4250 \pm 0.0091\,R_{\odot}$. The star TOI 762 A has a resolved binary star companion, TOI 762 B, that is separated from TOI 762 A by $3\farcs2$ (∼319 au) and has an estimated mass of $0.227 \pm 0.010\,M_{\odot}$. The planet TIC 46432937 b is a warm super-Jupiter with a mass of $3.20 \pm 0.11\,M_{\rm J}$ and radius of $1.188 \pm 0.030\,R_{\rm J}$. The planet's orbital period is $P = 1.4404$ days, and it undergoes grazing transits of its early M-dwarf host star, which has a mass of $0.563 \pm 0.029\,M_{\odot}$ and a radius of $0.5299 \pm 0.0091\,R_{\odot}$. TIC 46432937 b is one of the highest-mass planets found to date transiting an M-dwarf star. TIC 46432937 b is also a promising target for atmospheric observations, having the highest transmission spectroscopy metric or emission spectroscopy metric value of any known warm super-Jupiter (mass greater than $3.0\,M_{\rm J}$, equilibrium temperature below 1000 K).

Unified Astronomy Thesaurus concepts: Exoplanet systems (484); Exoplanet astronomy (486); Transit photometry (1709); Radial velocity (1332); Space telescopes (1547); M dwarf stars (982); Extrasolar gaseous giant planets (509)

Materials only available in the online version of record: machine-readable table

1. Introduction

How do the properties of giant planets depend on the masses of their host stars? This is a key open question and topic of current research in the field of exoplanets. Efforts to address

[28] Paris Region Fellow, Marie Sklodowska-Curie Action.

this question have been limited by the relatively small number of low-mass and high-mass stars that have been searched for planets compared to the much larger sample of solar-mass stars that have been searched to date by surveys like Kepler (W. J. Borucki et al. 2010) and TESS (G. R. Ricker et al. 2015).

In order to expand the sample of giant planets known around low-mass stars, we have been carrying out a program to follow-up candidate transiting giant planets around M-dwarf stars and late K-dwarf stars using the ESPRESSO instrument on the 8 m Very Large Telescope (VLT) at Paranal Observatory, in Chile. This facility has proven to be very efficient at gathering high-precision radial velocity (RV) observations for faint stars, even down to $V \sim 16.5$. We have so far published the confirmation of seven systems through this effort (J. D. Hartman et al. 2020; A. Jordán et al. 2022; J. M. Almenara et al. 2024; M. J. Hobson et al. 2023), and in this paper we publish the confirmation of two more such objects.

The planets that we confirm in this paper were identified by the NASA TESS mission, which has been carrying out a wide-field search for transiting planets around bright stars since its launch in 2018. Thanks to its all-sky observing strategy, the mission has also been successful at discovering the rare instances of transiting giant planets ($M_p > 0.1\,M_J$, for discussion purposes) around M-dwarf stars. A total of 17 of the 20 transiting giant planets that have been confirmed around M-dwarf stars so far were either first identified by TESS or included TESS follow-up observations as part of the discovery (C. I. Cañas et al. 2020, 2022, 2023; G. Á. Bakos et al. 2020; S. Kanodia et al. 2021, 2022, 2023; A. Jordán et al. 2022; T. Gan et al. 2022, 2023; A. H. M. J. Triaud et al. 2023; J. D. Hartman et al. 2023; M. J. Hobson et al. 2023; T. Kagetani et al. 2023). The three other known systems were discovered by Kepler (J. A. Johnson et al. 2012), HATSouth (J. D. Hartman et al. 2015), and NGTS (D. Bayliss et al. 2018).

While TESS has been very successful at discovering giant planets around M dwarfs, many of these objects were not identified through the mission's primary transit search effort operated by the Science Processing Operations Center (SPOC; J. M. Jenkins et al. 2016) at NASA's Ames Research Center (ARC), which focuses on the 2 minutes cadence observations, but were instead identified through special efforts to produce light curves for faint M-dwarf stars from the Full Frame Images (FFIs) and to search them for transit signals. One such effort is the TESS Faint-star Search (M. Kunimoto et al. 2022), which has identified some 3200 faint TESS Objects of Interest (TOIs) to date, including 128 candidate giant planets transiting M dwarfs. Another example is E. M. Bryant et al. (2023), who conducted a search for transiting giant planets around M dwarfs in 30 minutes cadence TESS observations and identified 15 candidates, including seven that were not previously identified by other projects. Both of the planets that we confirm in this paper were included in the E. M. Bryant et al. (2023) sample, and one of these systems (TIC 46432937 b) was first identified by them.

In the following section (Section 2), we discuss the observations that are used to confirm and characterize each planetary system. In Section 3, we describe the analysis methods. In Section 4, we discuss the results.

2. Observations

2.1. Initial Photometric Detection

Both TOI 762 A b and TIC 46432937 b were first identified as transiting planet candidates from observations gathered by the NASA TESS mission. Table 2 summarizes the TESS observations that are available for each system. Both targets were identified as candidates by an independent transit search performed by E. M. Bryant et al. (2023) with the aim of measuring the occurrence rates of giant planets with low-mass host stars. For this search the box-fitting least squares (BLS; G. Kovács et al. 2002) algorithm was utilized to search for giant planets transiting low-mass stars in light curves generated from the 30 minutes cadence FFIs from Cycle 1 of the TESS mission by the TESS-SPOC team (D. A. Caldwell et al. 2020). During Cycle 1 both TOI 762 A b and TIC 46432937 b were observed in a single sector: Sector 10 for TOI 762 A b (2019 March 29–2019 April 22) and Sector 6 for TIC 46432937 b (2018 December 15–2019 January 6). Following the BLS detection of these two candidates a number of automated checks were performed to investigate whether the transit-like signals could be the result of a number of different false-positive scenarios, such as eclipsing binaries or variable stars. See E. M. Bryant et al. (2023) for more details on the analyses performed. For both TOI 762 A b and TIC 46432937 b we found no evidence that the transit-like signals were a result of a nonplanetary scenario. An initial transit-fitting analysis was performed on both candidates using the BATMAN package (L. Kreidberg 2015) to generate the transit models and using EMCEE (D. Foreman-Mackey et al. 2013) to perform the Markov Chain Monte Carlo (MCMC) sampling. Both objects were identified as high-likelihood giant-planet candidates by this analysis and included in the sample reported in E. M. Bryant et al. (2023).

TOI 762 A b was independently identified as a candidate by the TESS-SPOC (J. M. Jenkins et al. 2016) at NASA ARC. The SPOC conducted a transit search of Sector 10 on 2019 May 23 with an adaptive, noise-compensating matched filter (J. M. Jenkins 2002; J. M. Jenkins et al. 2010, 2020), producing a threshold-crossing event for which an initial limb-darkened transit model was fitted (J. Li et al. 2019) and a suite of diagnostic tests were conducted to help make or break the planetary nature of the signal (J. D. Twicken et al. 2018). The transit signature was also detected in a search of FFI data by the Quick Look Pipeline at MIT (C. X. Huang et al. 2020a, 2020b). The TESS Science Office reviewed the vetting information and issued an alert on 2020 February 27 (N. M. Guerrero et al. 2021). The signal was repeatedly recovered as additional observations were made in Sectors 36, 37, and 63, and the transit signature passed all the diagnostic tests presented in the data validation reports. The difference image centroiding test located the host star within $3\farcs18 \pm 2\farcs58$ of the source of the transit signal.

The light curves used in the analysis of each system are summarized in Table 2. For TOI 762 A we make use of the 2 minutes cadence TESS light curves corrected for systematics by SPOC using the presearch data conditioning simple aperture photometry (PDCSAP) method of M. C. Stumpe et al. (2012, 2014) and J. C. Smith et al. (2012). For TIC46432937, we use the TESS-SPOC 30 and 10 minutes cadence light curves, which were also corrected using the PDCSAP method. All of the

Table 1
Sources within 10″ of TOI 762 A

Parameter	TOI 762 A	TOI 762 B	
Gaia DR3 ID	5362352744504000256	5362352744496315264	5362352744496318336
ΔR.A. (arcsec)	⋯	-2.754 ± 0.098	5.501 ± 0.092
Δdecl. (arcsec)	⋯	-1.62 ± 0.10	4.003 ± 0.092
$\mu_{\rm R.A.}$ (mas yr^{-1})	-159.174 ± 0.020	-157.37 ± 0.13	-5.15 ± 0.12
$\mu_{\rm decl.}$ (mas yr^{-1})	-24.780 ± 0.020	-24.38 ± 0.12	1.02 ± 0.11
π (mas)	10.118 ± 0.023	9.79 ± 0.14	0.40 ± 0.13
G (mag)	14.9297 ± 0.0028	18.1928 ± 0.0031	18.3444 ± 0.0030
BP − RP (mag)[a]	2.7548 ± 0.0059	3.554 ± 0.093	0.994 ± 0.020
$M_\star$ ($M_\odot$)	0.442 ± 0.025	0.227 ± 0.010	⋯

Note.
[a] We caution that the BP and RP photometry for each source appears to be contaminated by the other neighboring sources, as indicated by the high values of phot_bp_rp_excess_factor.

TESS light curves were obtained from the Mikulski Archive for Space Telescopes (MAST) at the Space Telescope Science Institute (STScI).

2.2. High-contrast Imaging

TOI 762 A was observed with the Zorro speckle imager on the Gemini-South 8 m telescope (N. J. Scott et al. 2021). Observations were obtained in the 832 ± 40 and 562 ± 54 nm bandpasses on 2020 January 11, and these were processed to generate reconstructed images following S. B. Howell et al. (2011). No companions to TOI 762 A were resolved through these observations within the field of view of Zorro, with contrast limits of $\Delta m_{832} > 5.42$ and $\Delta m_{562} > 4.9$ beyond 0.″5. Figure 1 shows the 832 nm reconstructed image, and the resulting 5σ magnitude contrast limits that we place on any companions to TOI 762 A.

There are two resolved sources within 10″ of TOI 762 A that are listed in the Gaia Data Release 3 (DR3) catalog (see also Table 1). Gaia DR3 5362352744496318336 is located 4.″7 to the northeast from TOI 762 A with $\Delta G = 3.42$ mag, $\Delta{\rm BP} = 2.29$ mag, and $\Delta{\rm RP} = 4.05$ mag relative to TOI 762 A. The parallax and proper motion of this object differ significantly from the values for TOI 762 A, indicating that the two sources are not physically associated. Gaia DR3 5362352744496315264 is located 3.″2 to the southwest of TOI 762 A and does appear to be physically bound to TOI 762 A with $\pi = 9.79 \pm 0.14$ mas, pmRA $= -157.37 \pm 0.13$ mas yr^{-1}, and pmDE $= -24.38 \pm 0.12$ mas yr^{-1} compared to $\pi = 10.118 \pm 0.023$ mas, pmRA $= -159.174 \pm 0.020$ mas yr^{-1}, and pmDE $= -24.780 \pm 0.020$ mas yr^{-1} for TOI 762 A.

Gaia DR3 5362352744496315264 has $\Delta G = 3.26$ mag, $\Delta{\rm BP} = 3.73$ mag, and $\Delta{\rm RP} = 2.93$ mag relative to TOI 762 A. This object has been identified as a wide binary companion to TOI 762 A in both the SUPERWIDE catalog (Z. D. Hartman & S. Lépine 2020) and the catalog of K. El-Badry et al. (2021). We refer to this star as TOI 762 B. Assuming this is a bound companion, we estimate that it is a late M-dwarf star with a mass of $0.227 \pm 0.010\,M_\odot$, at a projected physical separation of ∼319 au from TOI 762 A. The mass estimate is based on comparing the absolute G magnitude of the source to version 1.2 of the MIST theoretical stellar evolution models (B. Paxton et al. 2011, 2013, 2015; J. Choi et al. 2016; A. Dotter 2016), assuming the age, distance, metallicity, and reddening to the source are the same as for TOI 762 A. The inferred Two Micron All Sky Survey (2MASS) and Wide-field Infrared Survey Explorer (WISE) magnitudes for the star are $J = 14.057 \pm 0.086$ mag, $H = 13.475 \pm 0.076$ mag, $K_S = 13.177 \pm 0.085$ mag, $W_1 = 12.954 \pm 0.095$ mag, $W_2 = 12.71 \pm 0.10$ mag, $W_3 = 12.45 \pm 0.11$ mag, and $W_4 = 12.33 \pm 0.11$ mag. The measured relative proper-motion difference between TOI 762 A and TOI 762 B of $\Delta{\rm pm} = 1.85 \pm 0.13$ mas yr^{-1} is less than the value of 2.9 mas yr^{-1} that would be expected if the binary star system has a circular, face-on orbit, and suggests that the orbit is inclined and/or eccentric. We note that TOI 762 B is resolved from TOI 762 A in the spectroscopic observations (Section 2.4), which reveal a RV variation for TOI 762 A that is in phase with the transit ephemeris. Based on this, we conclude that TOI 762 A is the source of the transit signal.

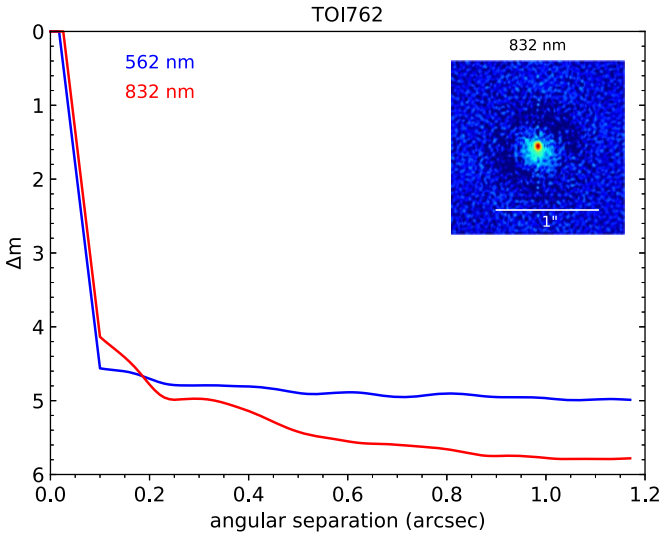

Figure 1. 5σ magnitude contrast limits for any companions to TOI 762 A based on Gemini/Zorro observations obtained in the 562 and 832 nm bandpass. The inset shows the reconstructed Gemini/Zorro image of TOI 762 A in the 832 nm bandpass.

The closer of the two neighbors is within the photometric aperture of the follow-up light curves for TOI 762 A, and would also have been unresolved in the 2MASS and WISE photometry of this source. The source is also close enough to be of concern for the Gaia BP and RP measurements. Using the relations in M. Riello et al. (2021) for the expected value and scatter of phot_bp_rp_excess_factor as functions of the BP − RP color and G magnitude for an isolated source, we

find that TOI 762 A has a value that is 3.3σ greater than expected. This indicates that these measurements may be contaminated; however, correcting for this contamination may be difficult to do accurately. For this reason we exclude the BP and RP photometry from the analysis of this system. We account for the contamination in the follow-up light curves as described in Section 3.3. To account for the contamination in the 2MASS and WISE photometry we use MIST v1.2 to estimate the apparent magnitude of the neighbor in these bandpasses given the absolute G magnitude, and assuming the age, metallicity, distance, and redenning to the source have the values that we determine for TOI 762 A. We then subtract the flux contribution of the neighbor from the observed 2MASS and WISE magnitudes, accounting for the uncertainty on the flux of the neighbor. These corrected magnitudes are listed in Table 5, and are also the values that we include in our analysis of the system (Section 3.3).

There are no nearby stars within $10''$ of TIC 46432937 listed in the Gaia DR3 catalog. Ground-based high-spatial-resolution imaging is not available for this target, so stellar companions within $1''$ cannot be ruled out.

2.3. Ground-based Photometric Follow-up

Ground-based photometric follow-up observations of TOI 762 A were obtained through the TESS Follow-up Observing Program (K. Collins 2019). Photometric follow-up observations of TIC 46432937 were also obtained. The observations that have been carried out for these systems are listed in Table 2. The data are shown in Figures 2 and 5, and are made available in Table 3. Here we briefly discuss each facility that was used.

2.3.1. LCOGT 1 m

A transit of TOI 762 A b was observed using a 1 m telescope at the Siding Spring Observatory, Australia station of the Las Cumbres Observatory Global Telescope (LCOGT) network (T. M. Brown et al. 2013). The observations were gathered through an I_C bandpass on 2019 June 28 using a SINISTRO imager. The images have a pixel scale of $0\farcs389\,\mathrm{px}^{-1}$, with an estimated average point-spread function (PSF) FWHM of $\sim 2''$. The data were reduced to ensemble-corrected light curves using the AstroImageJ package (K. A. Collins et al. 2017) with a photometric aperture radius of 14 pixels.

A separate photometric measurement was performed on the LCOGT images using a 2 pixel ($0\farcs8$) radius aperture to confirm that the transits are due to TOI 762 A rather than the neighbor TOI 762 B. This analysis revealed that TOI 762 A is indeed the source of the $\sim$30 ppt transit events.

2.3.2. ExTrA 0.6 m

A total of six transits of TOI 762 A b and six transits of TIC 46432937 b were monitored using the Exoplanets in Transits and their Atmospheres (ExTrA) facility (X. Bonfils et al. 2015) at La Silla Observatory in Chile. Several of the transits were simultaneously observed by more than one of the three 0.6 m telescopes in the facility, and for TIC 46432937 b we made multiband light curves from the observations, leading to a total of 14 separate transit light curves of TOI 762 A b and 64 separate light curves of TIC 46432937 b from this facility. The facility performs spectrophotometric observations over a wavelength range of 0.85–1.55 μm using a NIRvana 640 LN camera, which is fed with optical fibers from the three telescopes. Observations of TOI 762 A were gathered with the $4''$ diameter aperture fibers, except for on the night of 2021 March 13 when the $8''$ fibers were used. All transits of TIC 46432937 were observed with $8''$ diameter aperture fibers. Both targets were observed with the low-resolution mode of the spectrograph ($R \sim 20$). Bandpass-integrated, comparison-star-corrected light curves were produced following the method of M. Cointepas et al. (2021). For TOI 762 A we made use of light curves integrated over the full bandpass of the instrument, while for TIC 46432937, where the grazing transits make the solution more sensitive to limb darkening, we produced and analyzed separate Z-, Y-, J-, and H-band light curves from each transit observation.

2.3.3. TRAPPIST-South 0.6 m

Two transits of TOI 762 A b were observed using the southern 0.6 m TRAnsiting Planets and PlanetesImals Small Telescope (TRAPPIST-South; E. Jehin et al. 2011; M. Gillon et al. 2011; K. Barkaoui et al. 2019) at La Silla Observatory. The first transit on 2023 February 2 was observed through an $I+z$ filter, while the second transit on 2023 April 16 was observed through a z' filter. Observations were obtained at a pixel scale of $0\farcs64$. For the first transit the estimated PSF FWHM was $2\farcs6$ and a photometric aperture of $3\farcs84$ was used, while for the second transit the estimated PSF FWHM was $1\farcs4$ and a photometric aperture of $4\farcs48$ was used. Scheduling of the observations was performed using the tools of E. Jensen (2013), while ensemble-corrected light curves were derived from the observations following the methods of L. J. Garcia et al. (2022).

2.3.4. SPECULOOS-South 1.0 m

A transit of TOI 762 A b was observed on 2023 April 16 using three of the 1.0 m telescopes in the Search for habitable Planets EClipsing ULtra-cOOl Stars Southern observatory (SPECULOOS-South; L. Delrez et al. 2018; D. Sebastian et al. 2021; A. Y. Burdanov et al. 2022) at Paranal Observatory in Chile. Observations were gathered through the g', r', and z' filters. The observations had a pixel scale of $0\farcs35$ and an estimated PSF FWHM of $1\farcs6$. An aperture of radius $2\farcs45$ was used to extract the photometry. Scheduling of the observations was performed following D. Sebastian et al. (2021), while the data were reduced to ensemble-corrected light curves following C. A. Murray et al. (2020) and L. J. Garcia et al. (2021, 2022).

2.4. Spectroscopic Observations

Time-series spectroscopy was obtained for both TOI 762 A and TIC 46432937 using the ESPRESSO instrument (F. Pepe et al. 2021) on the 8 m VLT at Paranal Observatory in Chile. We obtained five observations of TOI 762 A in Period 104 between 2019 December 1 and 2019 December 24, and three observations in Period 110 between 2022 December 25 and 2022 December 30. We allow for an instrumental offset between the two periods in fitting the observations of TOI 762 A. For TIC 46432937, we obtained eight observations, all in Period 110, between 2022 November 24 and 2023 February 22. Observations were gathered in high-resolution mode (using a single unit telescope, and a spectroscopic resolution of $R \equiv \Delta\lambda/\lambda \sim 140{,}000$; the fiber aperture is $1''$ in this mode, and the wavelength coverage is from 3770 to

Table 2
Summary of Photometric Observations

Instrument/Field[a]	Date(s)	No. Images[b]	Cadence[c] (s)	Filter	Precision[d] (mmag)
TOI 762 A					
TESS/Sector 10	2019 Mar–2019 Apr	13,754	120	T	11.7
TESS/Sector 36	2021 Mar–2021 Apr	15,491	120	T	13.3
TESS/Sector 37	2021 Apr	15,061	120	T	13.9
TESS/Sector 63	2023 Mar–2023 Apr	17,456	120	T	12.5
LCOGT 1.0 m	2019 Jun 28	109	97	I_C	3.1
ExTrA—tel2	2021 Mar 13	214	62	0.85–1.55 μm	5.9
ExTrA—tel2	2021 Mar 27	168	62	0.85–1.55 μm	4.7
ExTrA—tel3	2021 Mar 27	164	62	0.85–1.55 μm	5.5
ExTrA—tel2	2021 Apr 24	159	62	0.85–1.55 μm	5.7
ExTrA—tel3	2021 Apr 24	160	62	0.85–1.55 μm	7.5
TRAPPIST-South	2023 Feb 2	214	83	$I+z$	3.5
ExTrA—tel1	2023 Apr 9	129	62	0.85–1.55 μm	7.3
ExTrA—tel2	2023 Apr 9	131	62	0.85–1.55 μm	4.8
ExTrA—tel3	2023 Apr 9	131	62	0.85–1.55 μm	5.0
SPECULOOS-South	2023 Apr 16	97	210	g'	3.2
SPECULOOS-South	2023 Apr 16	169	85	r'	3.2
SPECULOOS-South	2023 Apr 16	565	36	z'	2.9
ExTrA—tel1	2023 Apr 16	162	62	0.85–1.55 μm	7.4
ExTrA—tel2	2023 Apr 16	167	62	0.85–1.55 μm	4.4
ExTrA—tel3	2023 Apr 16	169	62	0.85–1.55 μm	5.4
TRAPPIST-South	2023 Apr 16	141	111	z'	3.0
ExTrA—tel1	2023 Apr 23	173	62	0.85–1.55 μm	11.2
ExTrA—tel2	2023 Apr 23	175	62	0.85–1.55 μm	6.1
ExTrA—tel3	2023 Apr 23	174	62	0.85–1.55 μm	8.7
TIC 46432937					
TESS/Sector 6	2018 Dec–2019 Jan	959	1800	T	1.2
TESS/Sector 32	2020 Nov–2020 Dec	3467	600	T	2.4
ExTrA—tel1	2023 Oct 10	141	62	Z	7.7
ExTrA—tel1	2023 Oct 10	141	62	Y	4.7
ExTrA—tel1	2023 Oct 10	140	62	J	4.3
ExTrA—tel1	2023 Oct 10	141	62	H	12.6
ExTrA—tel2	2023 Oct 10	140	62	Z	7.0
ExTrA—tel2	2023 Oct 10	140	62	Y	5.0
ExTrA—tel2	2023 Oct 10	140	62	J	4.3
ExTrA—tel2	2023 Oct 10	141	62	H	12.6
ExTrA—tel3	2023 Oct 10	141	62	Z	7.1
ExTrA—tel3	2023 Oct 10	141	62	Y	5.9
ExTrA—tel3	2023 Oct 10	141	62	J	5.3
ExTrA—tel3	2023 Oct 10	140	62	H	22.8
ExTrA—tel1	2023 Nov 5	165	62	Z	9.9
ExTrA—tel1	2023 Nov 5	165	62	Y	5.6
ExTrA—tel1	2023 Nov 5	165	62	J	5.2
ExTrA—tel1	2023 Nov 5	163	62	H	14.7
ExTrA—tel2	2023 Nov 5	163	62	Z	7.5
ExTrA—tel2	2023 Nov 5	165	62	Y	5.4
ExTrA—tel2	2023 Nov 5	165	62	J	5.3
ExTrA—tel2	2023 Nov 5	165	62	H	14.7
ExTrA—tel3	2023 Nov 5	165	62	Z	8.9
ExTrA—tel3	2023 Nov 5	165	62	Y	5.7
ExTrA—tel3	2023 Nov 5	164	62	J	6.0
ExTrA—tel3	2023 Nov 5	165	62	H	18.8
ExTrA—tel1	2023 Nov 18	269	62	Z	8.0
ExTrA—tel1	2023 Nov 18	268	62	Y	4.9
ExTrA—tel1	2023 Nov 18	269	62	J	4.6
ExTrA—tel1	2023 Nov 18	270	62	H	12.2
ExTrA—tel2	2023 Nov 18	269	62	Z	7.6
ExTrA—tel2	2023 Nov 18	269	62	Y	4.8
ExTrA—tel2	2023 Nov 18	268	62	J	4.5
ExTrA—tel2	2023 Nov 18	270	62	H	11.8
ExTrA—tel3	2023 Nov 18	269	62	Z	8.6
ExTrA—tel3	2023 Nov 18	268	62	Y	4.9
ExTrA—tel3	2023 Nov 18	269	62	J	5.2

Table 2
(Continued)

Instrument/Field[a]	Date(s)	No. Images[b]	Cadence[c] (s)	Filter	Precision[d] (mmag)
ExTrA—tel3	2023 Nov 18	269	62	*H*	14.8
ExTrA—tel1	2023 Dec 1	221	62	*Z*	8.1
ExTrA—tel1	2023 Dec 1	221	62	*Y*	5.8
ExTrA—tel1	2023 Dec 1	220	62	*J*	5.0
ExTrA—tel1	2023 Dec 1	220	62	*H*	11.8
ExTrA—tel2	2023 Dec 1	219	62	*Z*	8.0
ExTrA—tel2	2023 Dec 1	219	62	*Y*	5.6
ExTrA—tel2	2023 Dec 1	220	62	*J*	4.7
ExTrA—tel2	2023 Dec 1	220	62	*H*	15.1
ExTrA—tel3	2023 Dec 1	220	62	*Z*	9.0
ExTrA—tel3	2023 Dec 1	220	62	*Y*	5.9
ExTrA—tel3	2023 Dec 1	220	62	*J*	5.9
ExTrA—tel3	2023 Dec 1	221	62	*H*	16.4
ExTrA—tel1	2023 Dec 14	312	62	*Z*	8.3
ExTrA—tel1	2023 Dec 14	313	62	*Y*	5.3
ExTrA—tel1	2023 Dec 14	314	62	*J*	4.8
ExTrA—tel1	2023 Dec 14	313	62	*H*	15.8
ExTrA—tel3	2023 Dec 14	314	62	*Z*	8.2
ExTrA—tel3	2023 Dec 14	314	62	*Y*	5.6
ExTrA—tel3	2023 Dec 14	311	62	*J*	5.8
ExTrA—tel3	2023 Dec 14	313	62	*H*	15.9
ExTrA—tel1	2024 Jan 6	141	62	*Z*	8.6
ExTrA—tel1	2024 Jan 6	141	62	*Y*	5.2
ExTrA—tel1	2024 Jan 6	141	62	*J*	5.0
ExTrA—tel1	2024 Jan 6	140	62	*H*	12.7
ExTrA—tel3	2024 Jan 6	141	62	*Z*	8.7
ExTrA—tel3	2024 Jan 6	140	62	*Y*	5.7
ExTrA—tel3	2024 Jan 6	141	62	*J*	6.2
ExTrA—tel3	2024 Jan 6	140	62	*H*	16.4

Notes.
[a] For TESS data we list the sector from which the observations are taken.
[b] Excluding any outliers or other data not included in the modeling.
[c] The median time between consecutive images rounded to the nearest second. Due to factors such as weather, the day–night cycle, guiding and focus corrections, the cadence is only approximately uniform over short timescales.
[d] The rms of the residuals from the best-fit model. Note that in the case of TESS observations the transit may appear artificially shallower due to overfiltering and/or blending from unresolved neighbors. As a result the S/N of the transit may be less than what would be calculated from $R_p/R_\star$ and the rms estimates given here.

7910 Å). A sky fiber was placed 7″ from the target fiber, however there is no difference in the RVs derived from the sky-subtracted spectra compared to the non-sky-subtracted spectra due to the fact that moon contamination was minimal during the observations. An exposure time of 1800 s was used for the observations. For TOI 762 A the peak signal-to-noise ratio (S/N) varied from 23 to 30, while for TIC 46432937 the peak S/N was between 41 and 64.

The data were reduced to RV measurements in the solar system barycentric frame using the ESPRESSO Data Reduction Software (DRS) pipeline (v2.3.5; D. Sosnowska et al. 2015; A. Modigliani et al. 2020) in the EsoReflex environment (W. Freudling et al. 2013). The ESPRESSO DRS calculates the RVs from individual spectra by measuring the cross-correlation function (CCF) for each slice separately, using a template (stellar model) matching closest to the spectral type of the star. It then adds all these CCFs for the different orders, ignoring those orders that are severely affected by telluric contamination. It then fits a Gaussian function to the final CCF, where the center of the Gaussian is the RV and the width of the Gaussian represents the precision of the RV measurements.

Both systems show significant RV variations that are in phase with the transit ephemerides, and of amplitudes that indicate the transiting components are of planetary mass in both cases. The RV measurements for each system are shown in Figures 2 and 4 and are listed in Table 4.

3. Analysis

3.1. Derivation of Stellar Atmospheric Parameters

We used the machine-learning-based ODUSSEAS package (A. Antoniadis-Karnavas et al. 2020) to measure the photospheric effective temperature $T_{\rm eff\star}$ and metallicity [Fe/H] (assuming solar-scaled abundances) of both systems from the ESPRESSO spectra. The tool measures pseudo-equivalent widths for thousands of lines and compares them to a training set of reference M-dwarf stars observed by HARPS. Although the HARPS spectra have lower resolution than the ESPRESSO spectra, the tools has been shown to work effectively on high-resolution ESPRESSO spectra as well (J. Lillo-Box et al. 2020). The analysis was performed using the "wide error" mode, taking into consideration the intrinsic uncertainties of the reference parameters in the machine learning process in addition to the output machine learning model errors. We measure $T_{\rm eff\star} = 3150 \pm 67$ K and $[{\rm Fe/H}] = 0.24 \pm 0.10$ for

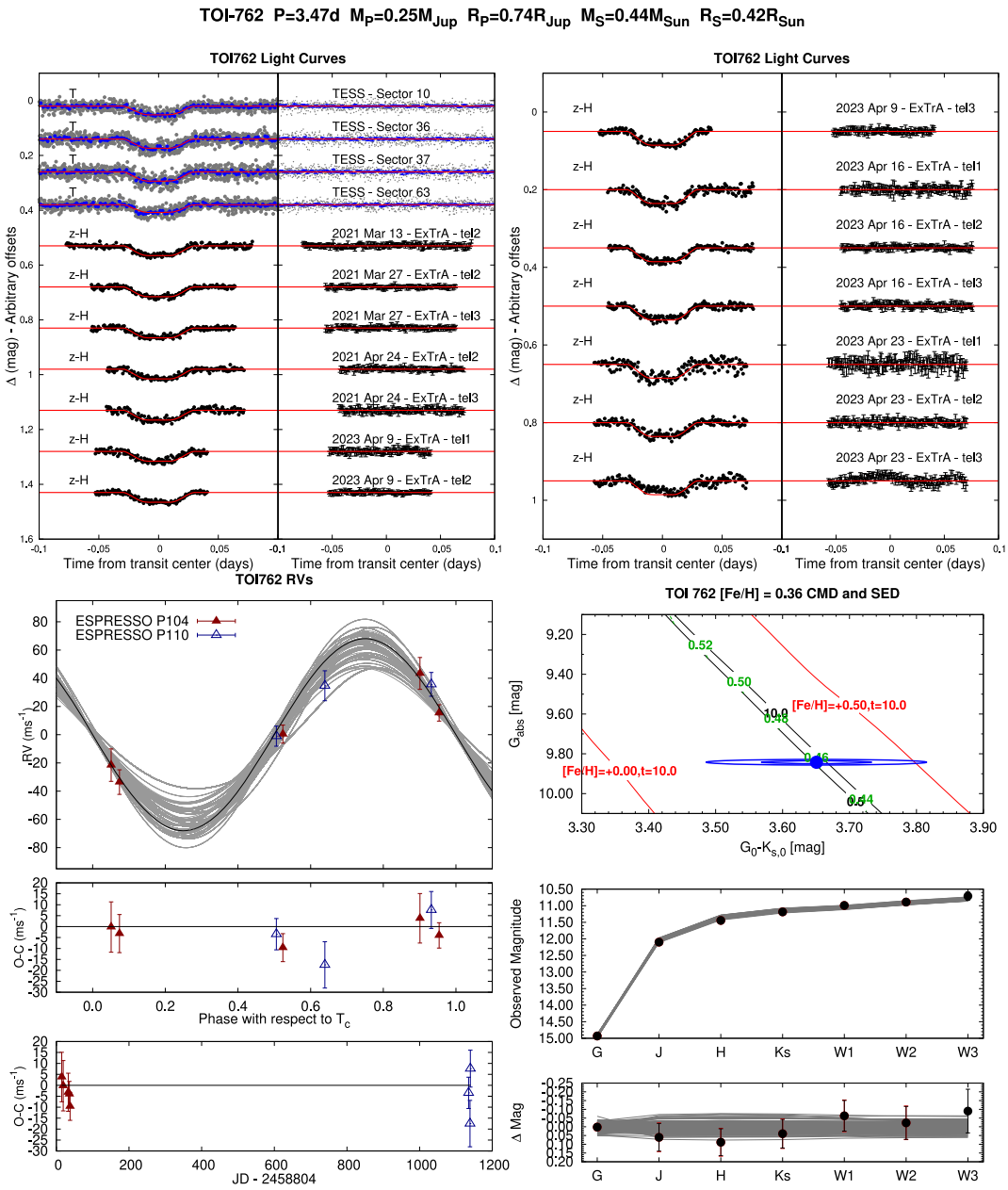

Figure 2. Observations incorporated into the analysis of the transiting planet system TOI 762 A. Additional light curves are shown in Figure 3. Top: transit light curves with best-fitted model (maximum likelihood) overplotted. The dates, filters, and instruments used are indicated. The term $z - H$ used for the ExTrA light curves refers to the full bandpass not the color. For TESS we phase-fold the data, and plot the unbinned observations in gray, with the phase-binned values overplotted in blue. The residuals for each light curve are shown on the right-hand side in the same order as the original light curves. The error bars represent the photon and background shot noise, plus the readout noise. Note that these uncertainties are scaled in the fitting procedure to achieve a reduced χ^2 of unity, but the uncertainties shown in the plot have not been scaled. Bottom left: high-precision RVs phased with respect to the mid-transit time. The top panel shows the phased measurements together with the best-fit (maximum-likelihood) model with no eccentricity. The grayscale curves show 1000 models randomly selected from the MCMC posterior distribution generated when the eccentricity is allowed to vary. The center-of-mass velocity has been subtracted. The middle panel shows the phase-folded velocity $O - C$ residuals. The error bars include the estimated jitter, which is varied as a free parameter in the fitting. The bottom panel shows the $O - C$ residuals as a function of time. Bottom right: color–magnitude diagram (CMD) and spectral energy distribution (SED). The top panel shows the absolute G magnitude vs. the dereddened $G - K_S$ color compared to theoretical isochrones (black lines) and stellar evolution tracks (green lines) from the MIST models interpolated at the best-estimate value for the metallicity of the host. The age of each isochrone is listed in black in billions of years, while the mass of each evolution track is listed in green in solar masses. The solid red lines show isochrones at higher and lower metallicities than the best-estimate value, with the metallicity and age in billions of years of each isochrone labeled on the plot. The filled blue circles show the measured reddening- and distance-corrected values from Gaia DR3 and 2MASS, while the blue lines indicate the 1σ and 2σ confidence regions, including the estimated systematic errors in the photometry. The middle panel shows the SED as measured via broadband photometry through the listed filters. Here we plot the observed magnitudes without correcting for distance or extinction. Overplotted are 200 model SEDs randomly selected from the MCMC posterior distribution produced through the global analysis (gray lines). The model makes use of the predicted absolute magnitudes in each bandpass from the MIST isochrones, the distance to the system (constrained largely via Gaia DR3), and extinction (constrained from the SED with a prior coming from the MWDUST 3D Galactic extinction model). The bottom panel shows the $O - C$ residuals from the best-fit model SED. The errors listed in the catalogs for the broadband photometry measurements are shown with black lines, while the errors including an assumed 0.02 mag systematic uncertainty, which is added in quadrature to the listed uncertainties, are shown with red lines. These latter uncertainties are what we use in the fit.

Table 3
Light-curve Data for TOI 762 A and TIC 46432937

Object[a]	BJD[b]	Mag[c]	$\sigma_{\rm Mag}$	Mag(orig)[d]	Filter	Instrument
TOI-762	2458595.24514	0.01246	0.01259	⋯	*T*	TESS/Sec10
TOI-762	2458577.88699	−0.00409	0.01237	⋯	*T*	TESS/Sec10
TOI-762	2458588.30220	−0.01125	0.01251	⋯	*T*	TESS/Sec10
TOI-762	2458581.35921	−0.01476	0.01231	⋯	*T*	TESS/Sec10
TOI-762	2458591.77437	−0.02359	0.01222	⋯	*T*	TESS/Sec10
TOI-762	2458574.41615	0.01873	0.01261	⋯	*T*	TESS/Sec10
TOI-762	2458595.24653	−0.01866	0.01228	⋯	*T*	TESS/Sec10
TOI-762	2458577.88838	−0.01855	0.01225	⋯	*T*	TESS/Sec10
TOI-762	2458588.30358	−0.00049	0.01260	⋯	*T*	TESS/Sec10
TOI-762	2458581.36059	−0.01694	0.01228	⋯	*T*	TESS/Sec10

Notes.
[a] Either TOI 762 A or TIC 46432937.
[b] Barycentric Julian Dates in this paper are reported on the Barycentric Dynamical Time (TDB) system.
[c] The out-of-transit level has been subtracted. For observations made with TESS these magnitudes have been corrected for trends *prior* to fitting the transit model. For observations made with follow-up instruments (anything other than "TESS" in the "Instrument" column), the magnitudes have been corrected for a quadratic trend in time fit simultaneously with the transit.
[d] Raw magnitude values without correction for the quadratic trend in time, or for trends correlated with the seeing. These are only reported for the follow-up observations.

(This table is available in its entirety in machine-readable form in the online article.)

TOI 762 A, and $T_{\rm eff\star} = 3535 \pm 65$ K and $[{\rm Fe/H}] = 0.03 \pm 0.10$ for TIC 46432937.

3.2. Stellar Activity and Galactic Kinematics

We checked the TESS light curves of TOI 762 A for evidence of stellar rotational variability or flaring events. No significant out-of-transit variability is observed. A total of six bright outliers ($>5\sigma$) are present in the out-of-transit TESS light curves of TOI 762 A. In each case the outlier is isolated to a single point, so if it is due to a flare, the flare would have been shorter than 120 s in duration. It is worth noting, though, that no 5σ faint outliers are detected. We also checked the publicly available ASAS-SN (B. J. Shappee et al. 2014; K. Hart et al. 2023) light curve TOI 762 A and see no evidence for periodic variability or stellar flares.

For TIC 46432937 a periodic signal is present in the out-of-transit TESS light curves from Sectors 6 and 32. We find a period of $P = 5.88 \pm 0.54$ days with a S/N of 35.2 as measured in the generalized Lomb–Scargle periodogram (M. Zechmeister & M. Kürster 2009). The estimated uncertainty on the period is the half-width at half-maximum of the peak in the periodogram. The peak-to-peak variation in the phase-binned light curve is ∼1 mmag. The formal false-alarm probability is vanishingly small, however this does not account for the possibility of systematic variations in the light curve due to uncorrected instrumental effects. We checked the Zwicky Transient Facility (ZTF; F. J. Masci et al. 2019) Data Release 20 light curve of TIC 46432937, but see no evidence for periodic variability. However, the scatter in the ZTF light curve of this source is ∼0.02 mag, and the ∼1 mmag amplitude signal seen in TESS would not be detectable if it is present in the ZTF data. No variability is detected in the publicly available ASAS-SN light curve of TIC 46432937 either, which also has too high a scatter to permit detection of a signal comparable to that seen in the TESS data. No candidate flare events or significant bright outliers are seen in the TESS light curve of TIC 46432937. While bright outliers are seen in the ZTF and ASAS-SN light curves, the number of faint outliers is comparable.

If the $P = 5.88$ days signal corresponds to the rotation period of TIC 46432937, the rotation period would be faster than the bulk of early M-dwarf stars with $0.9 < G - {\rm RP} < 1.1$ seen in the Kepler sample (A. McQuillan et al. 2014). While this may suggest a young age for TIC 46432937, existing gyrochronology relations are not suitable for M-dwarf stars (M. Popinchalk et al. 2021). It is also unclear how a relatively massive $\sim 3\,M_{\rm J}$ planet on a short $P = 1.44$ days orbit might affect the rotational evolution of an early M dwarf. For these reasons we do not attempt to estimate an age for TIC 46432937 based on the possible rotation period.

As an additional check on the ages of the systems, we used the systemic RVs that we measured for each star with ESPRESSO, together with the position, parallax, and proper motions from Gaia DR3 to compute the U, V, and W space velocities. We follow the convention that U increases toward the Galactic center, V increases in the direction of Galactic rotation, and W increases toward the north Galactic pole. These velocities are then corrected to be relative to the local standard of rest (LSR) by adding the solar peculiar velocities of $(U_\odot, V_\odot, W_\odot) = (11.10, 12.24, 7.25)\,{\rm km\,s^{-1}}$ from R. Schönrich et al. (2010). This yields $(U_{\rm LSR}, V_{\rm LSR}, W_{\rm LSR}) = (-35.56, -58.28, -22.96)\,{\rm km\,s^{-1}}$ and $(-73.82, -33.11, -31.21)\,{\rm km\,s^{-1}}$ for TOI 762 A and TIC 46432937, respectively. We use these velocities to compute the relative probabilities of each star being a member of the Galactic thin and thick disks, or of the Galactic halo, following T. Bensby et al. (2014). We find that both objects have a 70% probability of being members of the thin disk, a 30% probability of being members of the thick disk, and negligible probabilities of being members of the Galactic halo. While each object is more likely than not to be in the thin disk, both stars exhibit fairly high space motion compared to typical thin-disk members (both stars have at least one component of their space velocity that is different from the mean value for thin-disk stars by more

Table 4
ESPRESSO Radial Velocities for TOI 762 A and TIC 46432937

System	BJD (2450000+)	RV[a] ($m\ s^{-1}$)	σ_{RV}[b] ($m\ s^{-1}$)	Phase ($m\ s^{-1}$)	Instrument[c]
TOI-762	8818.82472	47.93	11.30	0.901	ESPRESSO/P104
TOI-762	8822.81705	−17.07	11.50	0.051	ESPRESSO/P104
TOI-762	8836.78307	−29.07	8.70	0.074	ESPRESSO/P104
TOI-762	8839.83846	19.93	5.80	0.954	ESPRESSO/P104
TOI-762	8841.81658	4.93	6.40	0.524	ESPRESSO/P104
TOI-762	9938.80622	3.43	7.14	0.506	ESPRESSO/P110
TOI-762	9942.74132	39.13	10.60	0.639	ESPRESSO/P110
TOI-762	9943.75858	40.13	8.42	0.932	ESPRESSO/P110
TIC-46432937	9907.75857	−423.38	1.95	0.086	ESPRESSO
TIC-46432937	9909.74414	−187.38	2.49	0.464	ESPRESSO
TIC-46432937	9928.64212	417.62	3.81	0.584	ESPRESSO
TIC-46432937	9930.76066	−277.38	1.94	0.054	ESPRESSO
TIC-46432937	9936.72836	−797.38	1.81	0.197	ESPRESSO
TIC-46432937	9995.60029	−336.38	3.53	0.068	ESPRESSO
TIC-46432937	9996.56963	836.62	2.08	0.741	ESPRESSO
TIC-46432937	9997.63070	−122.38	1.97	0.478	ESPRESSO

Notes.
[a] The zero-point of these velocities is arbitrary. An overall offset γ_{rel} fitted to the orbit has been subtracted for each system.
[b] Internal errors excluding the component of astrophysical jitter allowed to vary in the fit.
[c] For TOI 762 A we distinguish between the ESPRESSO observations obtained during P104 and those obtained during P110 for which we allow independent zero-point offsets in the fit.

than 2σ), which is consistent with both objects being older main-sequence stars.

3.3. Joint Stellar and Planet Modeling

We carried out a joint analysis of the available observations to determine the stellar and planetary parameters of each system following the method of J. D. Hartman et al. (2019) and G. Á. Bakos et al. (2020). For each object we performed a simultaneous fit to all light curves, RV measurements, the observed spectral energy distribution (SED) as traced by the available catalog broadband photometry, the spectroscopic $T_{\rm eff\star}$ and [Fe/H], and the astrometric parallax from Gaia DR3 (Gaia Collaboration et al. 2023). The catalog photometry, spectroscopic parameters, and parallax values that we included in the fit for each system are listed in Table 5. The light curves were modeled using the semi-analytic K. Mandel & E. Agol (2002) model with quadratic limb-darkening coefficients that were allowed to vary in the fit, but with priors based on the stellar atmospheric parameters in the theoretical tabulations by A. Claret et al. (2012, 2013) and A. Claret (2018). For the TESS observations of TIC 46432937, which have exposure times of 30 minutes or 10 minutes, we integrated the model over the exposure time. The RVs were fit assuming the star follows a Keplerian orbit around the system barycenter. The stellar parameters and SED are constrained to follow the MIST stellar evolution model while allowing for systematic errors in the stellar physical parameters following the procedure of J. D. Hartman et al. (2023). We adopt systematic errors of 0.08 dex, 2.4%, 5%, and 0.021 mag on the metallicity, effective temperature, stellar mass, and bolometric magnitudes in the stellar evolution models, respectively (J. Tayar et al. 2022). We impose a prior on the line-of-sight extinction A_V using the MWDUST 3D Galactic extinction model (J. Bovy et al. 2016) and assume an $R_V = 3.1$ extinction law. The fit is performed twice for each system, first assuming a circular orbit for the planet, and second allowing for a nonzero eccentricity. The fit is carried out through a differential evolution MCMC procedure (see J. D. Hartman et al. 2019, for a full list of parameters and priors) using visual inspection to confirm that the chains are converged and well mixed, and to set the burn-in period.

To account for dilution in the light curves of TOI 762 A due to the neighboring star TOI 762 B, we include for each light curve a parameter which specifies the fraction of the flux in the light curve that comes from the transit hosting star when out of transit (with the remaining fraction assumed to come from a constant source). This parameter is allowed to vary in the fit independently for each light curve. We place a prior and uncertainty on each of these dilution parameters by calculating the expected flux from TOI 762 B that would contaminate the aperture, assuming that TOI 762 B has the same distance, reddening, age, and metallicity as inferred for TOI 762 A, and using the G magnitude together with the MIST isochrones to infer the mass of TOI 762 B and its expected magnitude in various passbands. We note that the resulting dilution values are all consistent with the priors, to within the uncertainties. No systematic trend with wavelength is observed in the residuals.

The observations are consistent with circular orbits for both systems. For TOI 762 A b we place a 95% confidence upper limit on the eccentricity of $e < 0.083$, while for TIC46432937 b the upper limit is $e < 0.009$. We therefore adopt the parameters derived for each system assuming a circular orbit. Note that in the joint fitting that we perform the constraints on the eccentricities of these systems come not just from the RVs but also from the combination of the transit observations and the theoretical stellar evolution models that constrain the allowed combinations of stellar mass, radius, and metallicity. For M-dwarf host stars the constraints on mass and radius from comparing the observations to stellar evolution models are much tighter than for higher-mass stars, which can lead to a much tighter constraint on the eccentricity than might be allowed by the RVs alone (e.g., J. D. Hartman et al. 2015). This

Table 5
Astrometric, Spectroscopic, and Photometric Parameters for TOI 762 A and TIC 46432937

Parameter	TOI 762 A Value	TIC 46432937 Value	Source
Astrometric properties and cross-identifications			
2MASS-ID	11041818-4749169	05352856-1435504	
TIC-ID	178709444	46432937	
TOI-ID	762	…	
Gaia DR2-ID	5362352744504000256	2984391358868786816	
R.A. (J2000)	$11^h04^m18\overset{s}{.}1831$	$05^h35^m28\overset{s}{.}5693$	Gaia DR3
Decl. (J2000)	$-47°49'17\overset{''}{.}0030$	$-14°35'50\overset{''}{.}4600$	Gaia DR3
$\mu_{R.A.}$ (mas yr^{-1})	-159.174 ± 0.020	-13.365 ± 0.013	Gaia DR3
$\mu_{decl.}$ (mas yr^{-1})	-24.780 ± 0.020	36.962 ± 0.012	Gaia DR3
Parallax (mas)	10.118 ± 0.023	11.031 ± 0.013	Gaia DR3
Spectroscopic properties			
$T_{eff\star}$ (K)	3150 ± 67	3535 ± 65	See Section 3.1
[Fe/H]	0.24 ± 0.10	0.03 ± 0.10	See Section 3.1
γ_{RV} (m s^{-1})	48680.1 ± 4.3	102279.1 ± 2.5	ESPRESSO
Photometric properties[a]			
G (mag)[b]	14.9297 ± 0.0028	13.4172 ± 0.0028	Gaia DR3
BP (mag)[b]	…	14.4962 ± 0.0033	Gaia DR3
RP (mag)[b]	…	12.3785 ± 0.0039	Gaia DR3
B (mag)	…	15.707 ± 0.050	APASS[c]
V (mag)	…	14.310 ± 0.020	APASS[c]
g (mag)	…	15.040 ± 0.060	APASS[c]
r (mag)	…	13.740 ± 0.020	APASS[c]
i (mag)	…	12.792 ± 0.040	APASS[c]
J (mag)[d]	12.099 ± 0.080	11.011 ± 0.022	2MASS
H (mag)[d]	11.444 ± 0.077	10.427 ± 0.023	2MASS
K_s (mag)[d]	11.187 ± 0.082	10.195 ± 0.020	2MASS
$W1$ (mag)[e]	10.991 ± 0.088	10.114 ± 0.023	WISE
$W2$ (mag)[e]	10.890 ± 0.094	10.063 ± 0.020	WISE
$W3$ (mag)[e]	10.71 ± 0.12	9.910 ± 0.055	WISE

Notes.
[a] We only include in the table catalog magnitudes that were included in our analysis of each system.
[b] The listed uncertainties for the Gaia DR3 photometry are taken from the catalog. For the analysis we assume an additional systematic uncertainty of 0.02 mag for all bandpasses.
[c] From APASS Data Release 6 as listed in the UCAC 4 catalog (N. Zacharias et al. 2013). Although these measurements are also available for TOI 762 A, we do not include them in the analysis or list them here because the degree to which these measurements are contaminated by flux from the $3\overset{''}{.}2$ and $4\overset{''}{.}7$ neighbors is difficult to determine.
[d] From the 2MASS catalog (M. F. Skrutskie et al. 2006). For TOI 762 A we subtracted an estimate for the flux contribution from TOI 762 B.
[e] From the 2021 February 16 AllWISE Data release of the WISE mission (R. M. Cutri et al. 2021). For TOI 762 A we subtracted an estimate for the flux contribution from TOI 762 B.

appears to be the case for TOI 762 A b, for which the RVs alone provide a much less stringent constraint on the eccentricity than is achieved through our joint analysis of the data. For TIC 46432937 b, on the other hand, the eccentricity constraint appears to come primarily from the RVs. Here the large semi-amplitude of the orbital variation caused by the massive planet and the well-sampled phase curve enable a strong constraint on the orbital eccentricity.

We find that TIC 46432937 b exhibits grazing transits, which in some cases can lead to a strong degeneracy between the impact parameter of the planet and the planet-to-star radius ratio. In such cases it may only be possible to provide a lower bound on the planetary radius (e.g., HATS-23 b; J. Bento et al. 2017). We confirmed that the Markov Chains for TIC46432937 are well converged and display a clear upper limit on both the impact parameter and the planet-to-star radius ratio, so we provide best estimates for these parameters together with two-sided uncertainties.

Figures 2–5 compare the best-fit models to the observational data. The adopted stellar parameters are listed in Table 6, while the adopted planetary parameters are listed in Table 7 and the limb-darkening coefficients are listed in Table 8. In both cases we list the parameters determined assuming circular orbits.

3.4. Ruling Out Blended Stellar Eclipsing Binary Scenarios

A line-of-sight blend of three stars, including two that are eclipsing, is a relatively common false positive that can mimic the photometric transit and RV signals produced by a transiting giant-planet system (e.g., G. Torres et al. 2004). In order to rule out such an explanation for the observations of TOI 762 A or TIC 46432937 we carried out a blend analysis following the methods of J. D. Hartman et al. (2019). Here we model the photometric and astrometric data as a blend of three or more stars using the MIST version 1.2 stellar evolution models to constrain the physical properties of the stars. We consider both a hierarchical triple star system, where the two fainter stars in the system are eclipsing, and a line-of-sight blend between an eclipsing binary star system and a brighter, physically unrelated, foreground star.

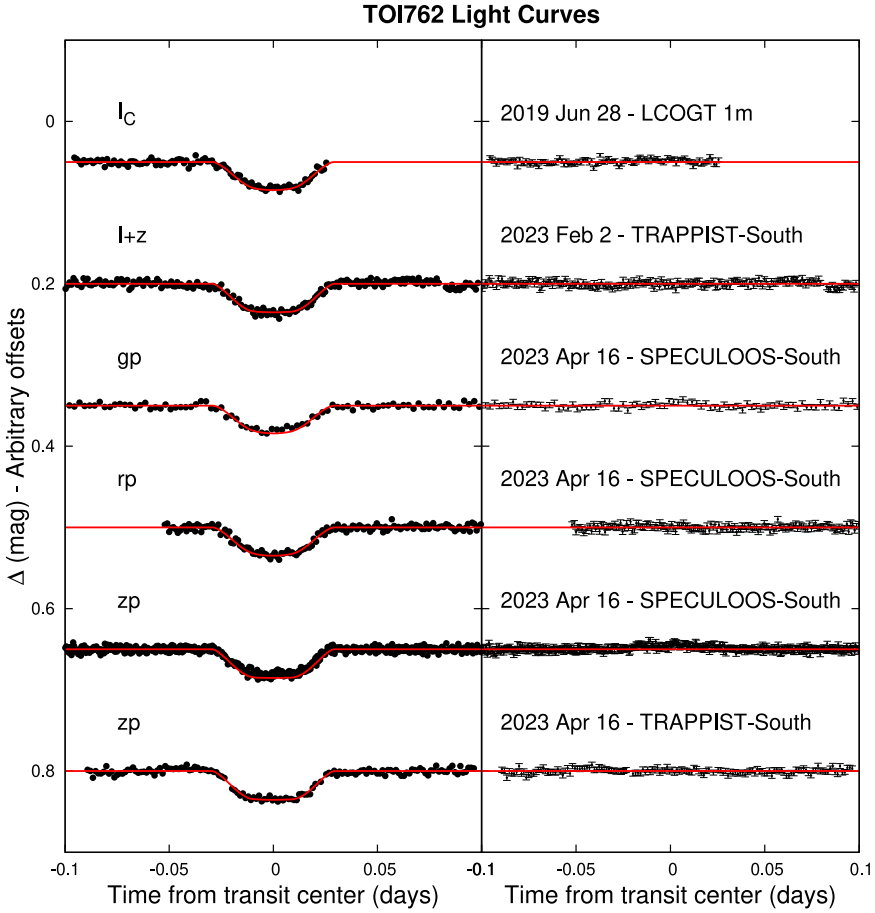

Figure 3. Additional follow-up light curves of TOI 762 A, shown as described in Figure 2.

For TIC 46432937, the analysis was performed before the photometric follow-up observations were available, and only the TESS light curves are included in this case. Because the parameters that were measured for the system when using only the TESS observations are fully consistent with the parameters found when incorporating the follow-up light curves from ExTrA, and as we discuss below we can already rule out blend scenarios with only the TESS data, we do not expect the conclusions from the blend analysis to change when incorporating the follow-up light curves. We therefore did not repeat the blend analysis for this system after obtaining the light curves from ExTrA.

For the hierarchical triple system, the parameters that we vary in the fit include the times of two reference transit events, the age of the stellar system, the masses of the three stellar companions, the distance to the system, the metallicity of the system, the impact parameter of the eclipsing pair, and the limb-darkening coefficients of the primary star in the eclipsing pair. For the line-of-sight blend we include all of these parameters, as well as the age, metallicity, and distance of the blended foreground star. We compare both of these scenarios to a model consisting of a transiting planet around a single star for which we vary the system age, metallicity and distance, the mass and limb-darkening coefficients of the host star, the impact parameter of the system, and the planet-to-star radius ratio.

For TOI 762, we also account for the 3.″2 resolved stellar components TOI 762 A and TOI 762 B in modeling the observations, and attempt to model the brighter target TOI 762 A, for which RV variations consistent with a planetary companion were detected, as a blended system of three stars. Thus for TOI 762 there are four stars considered in the blend scenarios that we investigate, and we include the mass of the 3.″2 neighbor TOI 762 B as a parameter in the fit, and assume that this neighbor has the same age, metallicity, and distance as the brightest star in the blended object TOI 762 A.

We find that for both TOI 762 and TIC 46432937 the transiting planet scenario provides a significantly better fit to the photometric and astrometric data, with lower χ^2, than the blended stellar eclipsing binary systems that we considered. For TOI 762 we find that the best-fit transiting planet model has $\Delta\chi^2 = -305$ compared to the best-fit blended eclipsing binary model, while for TIC 46432937 we find $\Delta\chi^2 = -287$. As the transiting planet scenarios also require fewer free parameters, we can confidently rule out a blended stellar eclipsing binary system for both objects. The best-fit blend scenarios exhibit secondary eclipses that are ruled out by the TESS observations, as well as distances and implied apparent magnitudes for the blended objects that are inconsistent with the Gaia parallax and measured apparent magnitudes. We therefore consider both objects to be confirmed transiting planet systems.

4. Discussion

In this paper, we presented the discovery of two transiting giant planets that orbit M-dwarf stars. Figure 6 compares these two new systems to other confirmed transiting planet systems listed in the NASA Exoplanet Archive (2024).[29] We find that

[29] Accessed on 2024 January 17 at 12:40.

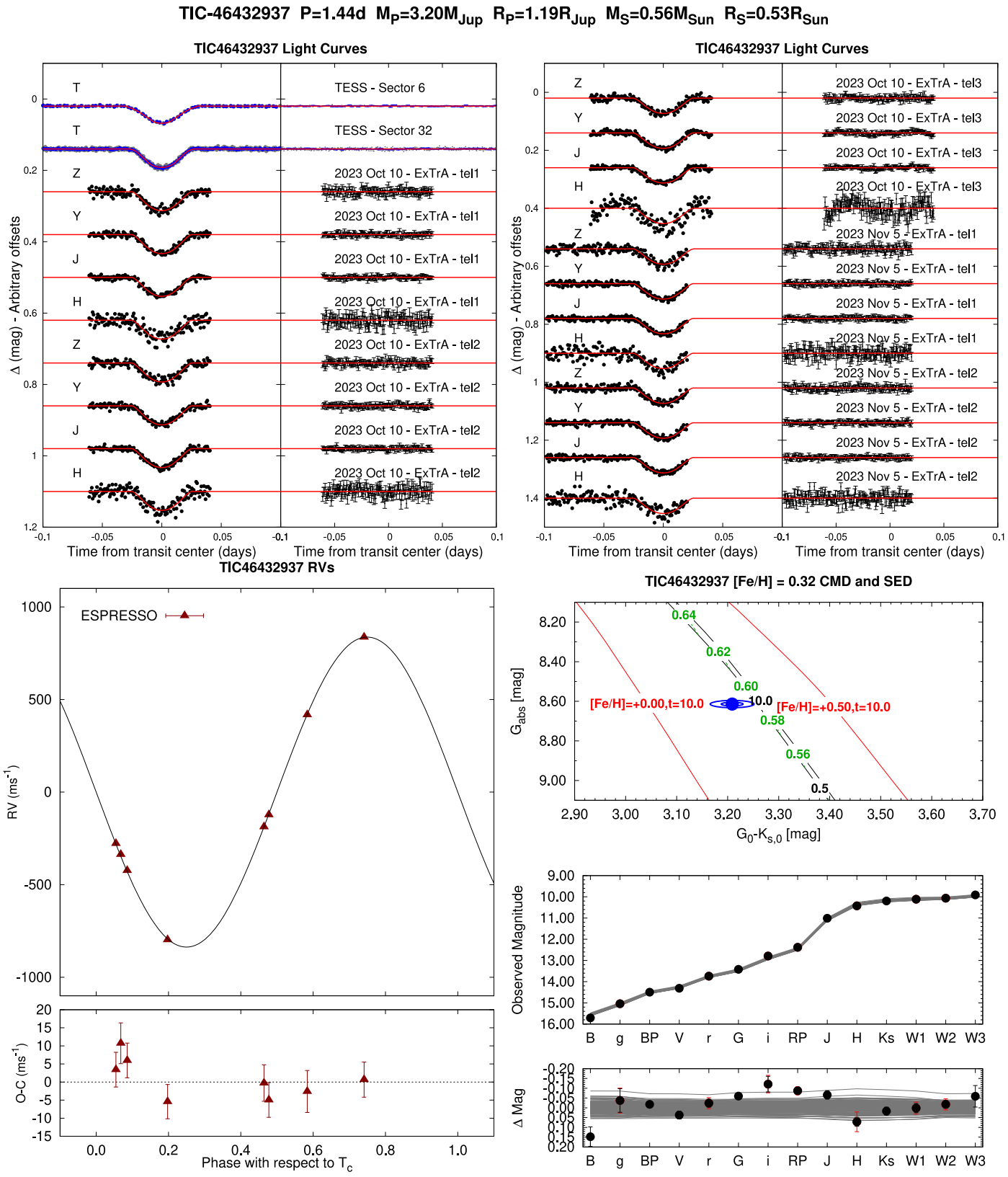

Figure 4. Same as Figure 2, here we show the observations of TIC 46432937 together with our best-fit model. Additional follow-up light curves of TIC 46432937 are shown in Figure 5.

with $M_\star = 0.442 \pm 0.025\,M_\odot$, TOI 762 A is one of the lowest-mass stars known to host a transiting giant planet (taking $M_p > 0.1\,M_J$ as our definition of such a planet; it is also one of the lowest-mass stars known to host a giant planet in general), while with $M_p = 3.20 \pm 0.11\,M_J$, TIC 46432937 b is one of the highest-mass planets known to transit an M-dwarf star. Stars of lower mass than TOI 762 A with giant planets include TOI-4860 ($0.336\,M_\odot$; A. H. M. J. Triaud et al. 2023), TOI-519

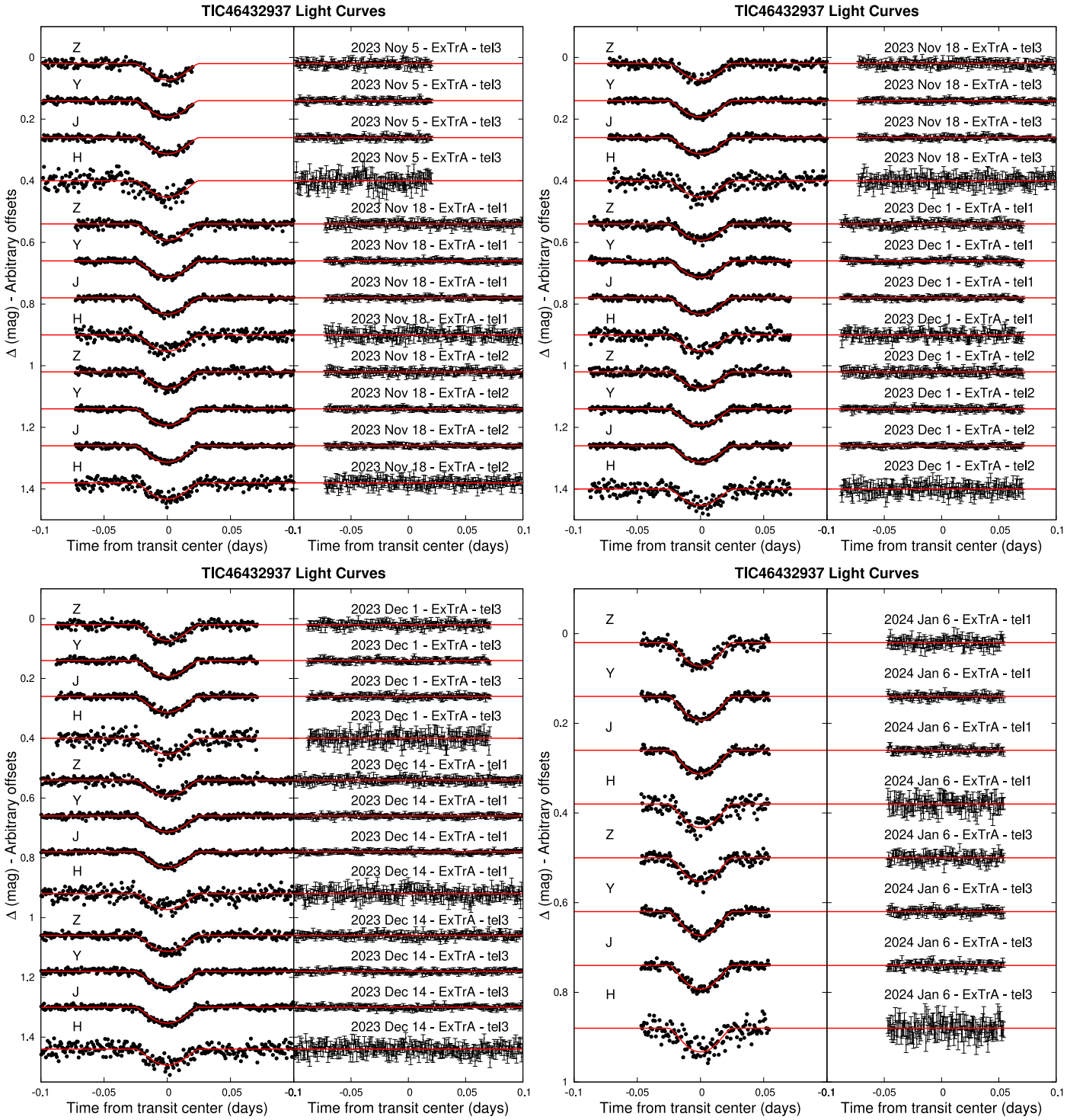

Figure 5. Additional follow-up light curves of TIC 46432937, shown as described in Figure 2.

(0.335 $M_\odot$; T. Kagetani et al. 2023), TOI-5205 (0.392 $M_\odot$; S. Kanodia et al. 2023), and TOI-3235 (0.370 $M_\odot$; M. J. Hobson et al. 2023). The only transiting object orbiting an M-dwarf star listed on the NASA Exoplanet Archive with a higher mass than TIC 46432937 b is TOI-1278 b (É. Artigau et al. 2021), but with a mass of $18.5 \pm 0.5\,M_J$, this object may be a brown dwarf rather than a planet. The next highest mass planet is TOI-4201 b (2.48 M_J; J. D. Hartman et al. 2023; M. Delamer et al. 2024; T. Gan et al. 2023).

Stellar companion to TOI 762 A. We find that TOI 762 A has a resolved stellar companion TOI 762 B. The angular separation of 3.″2 between the two stars corresponds to a current projected physical separation of 319 au. We estimate that TOI 762 B has a mass of $0.227 \pm 0.010\,M_\odot$, which is 45% the mass of TOI 762 A. The eccentricity and orbital period of TOI 762 B are not known.

If the eccentricity is sufficiently high, then TOI 762 B might have induced high-eccentricity migration for the planet

Table 6
Adopted Derived Stellar Parameters for TOI 762 A and TIC 46432937

Parameter	TOI 762 A Value	TIC 46432937 Value
$M_\star$ ($M_\odot$)	0.442 ± 0.025	0.563 ± 0.029
$R_\star$ ($R_\odot$)	0.4250 ± 0.0091	0.5299 ± 0.0091
$\log g_\star$ (cgs)	4.827 ± 0.010	4.740 ± 0.010
$\rho_\star$ (g cm^{-3})	8.11 ± 0.20	5.34 ± 0.11
$L_\star$ ($L_\odot$)	0.0185 ± 0.0011	0.0412 ± 0.0031
$T_{\rm eff\star}$ (K)	3266 ± 36	3572 ± 57
[Fe/H]	0.357 ± 0.085	0.323 ± 0.081
Age (Gyr)	9.3 ± 5.5	7.4 ± 5.1
A_V (mag)	0.1740 ± 0.0052	0.023 ± 0.012
Distance (pc)	98.78 ± 0.22	90.64 ± 0.10

Note. The listed parameters are those determined through the joint differential evolution Markov Chain analysis, including systematic errors in the stellar evolution models, described in Section 3.3. For all systems the RV observations are consistent with a circular orbit, and we assume a fixed circular orbit in generating the parameters listed here.

TOI 762 A b via the Kozai–Lidov mechanism (M. L. Lidov 1962; Y. Kozai 1962; S. Naoz 2016). To get a rough sense for the timescale of this mechanism we use Equation (7) of L. G. Kiseleva et al. (1998), assuming that the current projected physical separation corresponds to the semimajor axis of the orbit of the binary star system. We find a timescale of ~100 Myr if TOI 762 B has a very high eccentricity of 0.95, or ~3.5 Gyr if the eccentricity is close to zero.

Four other M dwarfs that host transiting giant planets also have known wide stellar binary companions: TOI 3984 A (C. I. Cañas et al. 2023), TOI 5293 A (C. I. Cañas et al. 2023), TOI 3714 (C. I. Cañas et al. 2022), and HATS-74 A (A. Jordán et al. 2022). Thus approximately 20% of the sample of M dwarfs with transiting giant planets are known to have resolved stellar binary companions. The overall stellar multiplicity fraction for M-dwarf stars is estimated to be $46\% \pm 5\%$ (N. Susemiehl & M. R. Meyer 2022); however, a meaningful comparison to the rate for giant-planet host stars will require a careful correction for observational completeness. Such a study will likely require a much larger sample of giant-planet-hosting M dwarfs to enable a statistically significant result.

H. Ngo et al. (2016) compare the stellar multiplicity rate for FGK stars that host hot Jupiters to the rate for field FGK stars. They find that the fraction of hot Jupiter systems with stellar companions between 50 and 2000 au is approximately 2.9 times the field star companion fraction. But they also find that, in the majority of cases, the stellar binary companions could not drive high-eccentricity migration through the Kozai–Lidov effect. They conclude that for FGK systems binarity is likely correlated with the formation of hot Jupiters, but the binary companions themselves do not physically drive their migration.

High mass of TIC 46432937 b. The high mass of TIC 46432937 b given its low stellar host mass of $0.563 \pm 0.029\,M_\odot$ poses a challenge for theories of planet formation and evolution. T. Gan et al. (2023) carried out interior structure modeling of the planet TOI-4201 b, which has a similar radius to TIC 46432937 b, similar host-star metallicity and similar planet equilibrium temperature, but somewhat lower planet mass and somewhat larger host-star mass. They find that TOI-4201 b requires a low planet bulk metal content which appears to be at odds with the high metallicity inferred for the host star. Given the higher planet mass of TIC 46432937 b, the comparably high metallicity of its host star, and the comparable planet radius and equilibrium temperature, we anticipate that a similar analysis would result in the same conclusion for TIC 46432937 b as T. Gan et al. (2023) arrived at for TOI-4201 b, i.e., that the planet mass/radius/equilibrium temperature requires a low planet bulk metal content that is at odds with the high host-star metallicity. T. Gan et al. (2023) consider a variety of potential heating sources that might explain the discrepancy, including tidal heating (J. Leconte et al. 2010), a gas giant merger (S. L. Li et al. 2010; S.-F. Liu et al. 2015), and a more quiescent process involving an embryo being captured by a gas giant during inward migration (D. N. C. Lin et al. 1996). The fact that two super-Jupiter-mass planets have now been found around M-dwarf stars with somewhat high radii, suggesting low bulk metal content, indicates that if there is an additional heating mechanism it may be common for short-period giant planets around M-dwarf stars. With only two planets, however, we cannot draw any definite conclusions at this point.

Grazing transients of TIC 46432937 b. We find that TIC 46432937 b exhibits grazing transit events. Two other giant planets around M dwarfs have been found with grazing transits: NGTS 1 b (D. Bayliss et al. 2018) and the super-massive planet or brown dwarf TOI 1278 B (É. Artigau et al. 2021). The relatively large values of $R_p/R_\star$ for giant planets orbiting M dwarfs enhances the probability of finding these systems in grazing configurations compared to giant planets transiting Sun-like stars. The deep V-shaped transit events exhibited by these systems are often considered the hallmark of stellar eclipsing binaries, so it is important to keep in mind that transiting planets can have light curves of this form as well when searching for giant planets transiting M-dwarf stars.

Because grazing transit events do not have second or third contact points (the times when a planet starts and stops being fully in front of its host star, respectively), there is less information content in a grazing transit than in a full transit event. This can lead to degeneracies between the impact parameter and the planet-to-star radius ratio, resulting in larger uncertainties on the planetary radius and other parameters for these systems. High-precision observations, such as from TESS, can help break this degeneracy and enable an accurate measurement of the planetary radius in spite of the grazing transits. We find that this is the case for TIC 46432937 b, for which we find that the radius is measured to 2.5% uncertainty despite the grazing events.

One minor advantage of a grazing system is that secular variations in the orbits of these planets, due for example to the presence of exterior planets in the system, may be detectable with higher S/N than for full transits (I. Ribas et al. 2008). An example of this is K2-146 c, a planet whose orbit has been seen to vary between grazing and fully transiting configurations (A. Hamann et al. 2019). While no timing variations have been detected yet for TIC 46432937 b, the grazing transits make this an interesting target for continued transit timing observations going forward.

Prospects for atmospheric characterization. Transiting giant planets orbiting M-dwarf stars can be useful objects for atmospheric characterization due to their relatively deep transits.

Table 7
Adopted Orbital and Planetary Parameters for TOI 762 A b and TIC 46432937 b

Parameter	TOI 762 A b Value	TIC 46432937 b Value
Light-curve parameters		
P (days)	$3.47168260 \pm 0.00000072$	$1.440445270 \pm 0.000000087$
T_c (BJD_TDB)[a]	$2459850.258470 \pm 0.000094$	$2459952.288940 \pm 0.000039$
T_{14} (days)[a]	0.05789 ± 0.00031	0.04981 ± 0.00026
$T_{12} = T_{34}$ (days)[a]	0.01877 ± 0.00048	…
$\phi_{\rm occ}$ (phase)[b]	0.513 ± 0.018	0.50064 ± 0.00093
$T_{c,\rm occ}$ (BJD_TDB)[b]	2459876.341 ± 0.062	2460009.1874 ± 0.0013
$T_{14,\rm occ}$ (days)[b]	0.05759 ± 0.00067	0.05237 ± 0.00073
$a/R_\star$	17.29 ± 0.14	8.381 ± 0.056
$\zeta/R_\star$[c]	47.79 ± 0.30	$64.73^{+2.37}_{-0.89}$
$R_p/R_\star$	0.17985 ± 0.00095	0.2301 ± 0.0037
b^2	$0.5710^{+0.0086}_{-0.0101}$	$0.681^{+0.026}_{-0.012}$
$b \equiv a\cos i/R_\star$	$0.7556^{+0.0057}_{-0.0067}$	$0.8250^{+0.0157}_{-0.0073}$
i (deg)	87.500 ± 0.039	$84.350^{+0.090}_{-0.140}$
RV parameters		
K (m s^{-1})	58.1 ± 9.3	837.1 ± 4.4
e[d]	<0.083	<0.009
RV jitter ESPRESSO 1 (m s^{-1})[e]	0.1 ± 4.1	5.3 ± 2.5
RV jitter ESPRESSO 2 (m s^{-1})[e]	0.0 ± 2.9	…
Planetary parameters		
M_p ($M_{\rm J}$)	0.251 ± 0.042	3.20 ± 0.11
R_p ($R_{\rm J}$)	0.744 ± 0.017	1.188 ± 0.030
C (M_p, R_p)[f]	0.17	0.53
ρ_p (g cm^{-3})	0.76 ± 0.13	2.37 ± 0.15
$\log g_p$ (cgs)	3.053 ± 0.072	$3.751^{+0.016}_{-0.023}$
a (au)	0.03418 ± 0.00065	0.02065 ± 0.00035
$T_{\rm eq}$ (K)	555.4 ± 6.4	872 ± 14
Θ[g]	0.0523 ± 0.0085	0.1951 ± 0.0051
$\log_{10}\langle F\rangle$ (cgs)[h]	7.334 ± 0.020	8.119 ± 0.028

Notes. For both systems we adopt a model in which the orbit is assumed to be circular. Except where noted otherwise, the listed parameters are calculated assuming circular orbits. See the discussion in Section 3.3.

[a] Times are in Barycentric Julian Date calculated on the Barycentric Dynamical Time (TDB) system. T_c: reference epoch of mid-transit that minimizes the correlation with the orbital period. T_{14}: total transit duration, time between first to last contact; $T_{12} = T_{34}$: ingress/egress time, time between first and second, or third and fourth contact.

[b] Inferred timing of occultation events calculated from the fit where the eccentricity is allowed to vary. Occultations have not been observed for either system. Times are in Barycentric Julian Date calculated on the Barycentric Dynamical Time (TDB) system. $\phi_{\rm occ}$: orbital phase of the occultation; phase 0 refers to the time of mid-transit. $T_{c,\rm occ}$: reference epoch of mid occultation. $T_{14,\rm occ}$: total occultation duration.

[c] Reciprocal of the half duration of the transit used as a jump parameter in our MCMC analysis in place of $a/R_\star$. It is related to $a/R_\star$ by the expression $\zeta/R_\star = a/R_\star(2\pi(1 + e\sin\omega))/(P\sqrt{1-b^2}\sqrt{1-e^2})$ (G. Á. Bakos et al. 2010).

[d] The 95% confidence upper limit on the eccentricity determined when $\sqrt{e}\cos\omega$ and $\sqrt{e}\sin\omega$ are allowed to vary in the fit.

[e] Term added in quadrature to the formal RV uncertainties for each instrument. This is treated as a free parameter in the fitting routine. The two values listed for TOI 762 A b are for the ESPRESSO P104 and P110 data, respectively.

[f] Correlation coefficient between the planetary mass M_p and radius R_p estimated from the posterior parameter distribution.

[g] The Safronov number is given by $\Theta = \frac{1}{2}(V_{\rm esc}/V_{\rm orb})^2 = (a/R_p)(M_p/M_\star)$ (see B. M. S. Hansen & T. Barman 2007).

[h] Incoming flux per unit surface area, averaged over the orbit.

We computed the transmission spectroscopy metric and emission spectroscopy metric (TSM and ESM, respectively; E. M. R. Kempton et al. 2018) for the two new planetary systems presented here, finding values of TSM = 101 ± 21 and ESM = 18.3 ± 1.5 for TOI 762 A b, and TSM = 52.3 ± 4.8 and ESM = 152 ± 11 for TIC 46432937 b. These are compared to other transiting giant planets from the NASA Exoplanet Archive in Figure 7. While neither of the newly discovered planets has an especially high TSM value compared to the overall sample of transiting giant planets, their values are both greater than the median value of TSM = 47.4 for the full sample of confirmed warm transiting giant planets with equilibrium temperatures $T_{\rm eq} < 1000$ K. When comparing against planets of $M_p > 3.0\,M_{\rm J}$, the TSM of TIC 46432937 b does stand out as being greater than the value for all but four of these planets (i.e., it has a greater TSM value than 92% of all known transiting planets with $M_p > 3.0\,M_{\rm J}$). These four planets, HAT-P-70 b (TSM = 57.8; G. Zhou et al. 2019), MASCARA-4 b (TSM = 107; P. Dorval et al. 2020), TOI-1431 b (TSM = 109; B. C. Addison et al. 2021), and HIP 65 A b (TSM = 780; L. D. Nielsen et al. 2020), all have equilibrium temperatures greater than 1400 K, which is significantly higher than that of

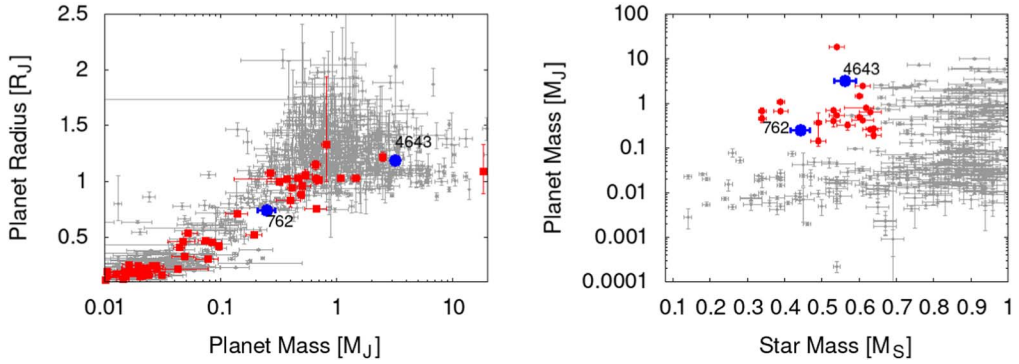

Figure 6. Left: planet radius vs. mass. The two new planet discoveries are indicated (we abbreviate TIC 46432937 b as 4643). Small gray points show all transiting planets with measured masses and radii around K- and earlier-type stars from the NASA Exoplanet Archive, while red points show transiting planets with masses and radii around M dwarfs. Right: planet mass vs. host-star mass for transiting planets around subsolar-mass stars. The red points in this case indicate giant planets transiting M dwarfs, while the gray points indicate other planets.

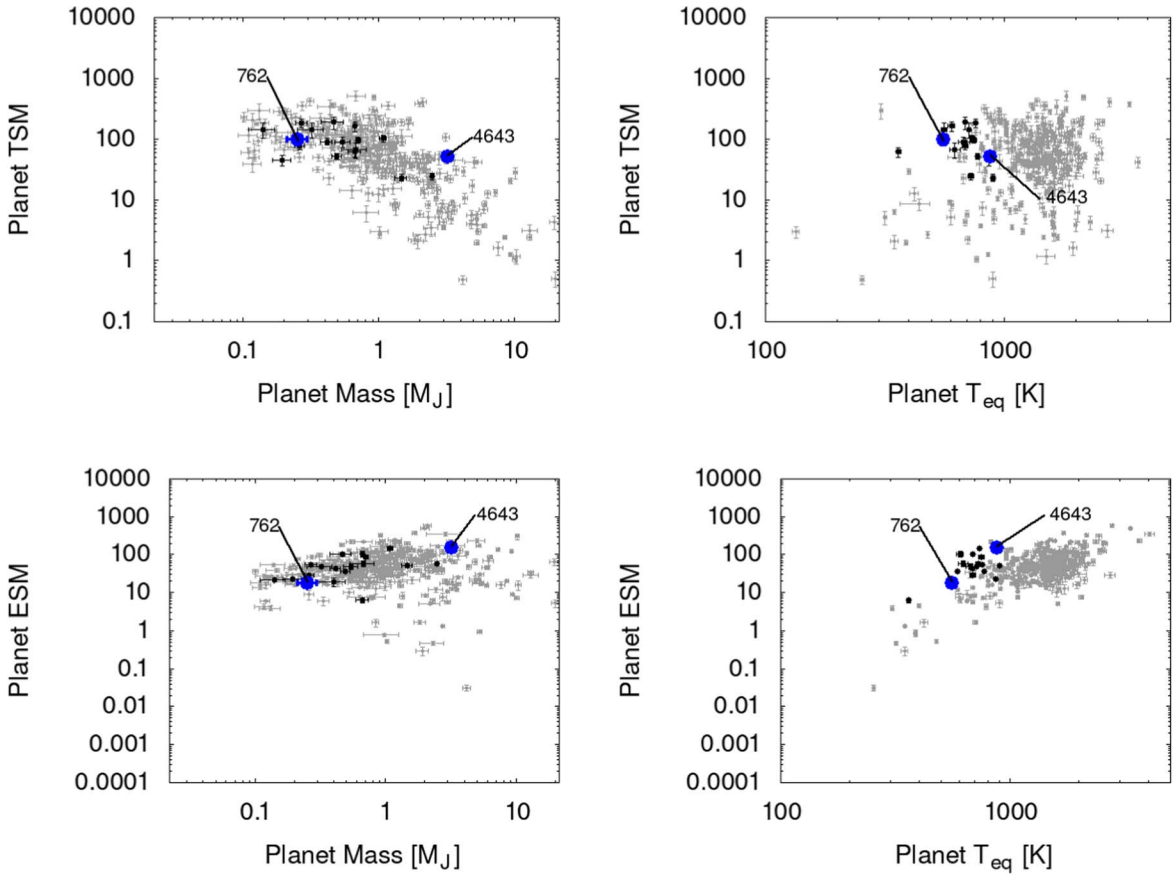

Figure 7. Top left: transmission spectroscopy metric (TSM) vs. planet mass. TOI 762 A b and TIC 46432937 b are indicated. Small gray points show all transiting planets with measured masses >0.1 M_J and radii >0.5 R_J from the NASA Exoplanet Archive, while small black points denote planets with M-dwarf host stars. For all panels we restrict the plots to planets for which the plotted quantities have uncertainties of less than 30%. Top right: TSM vs. planet T_{eq} computed assuming zero albedo and full redistribution of heat. The symbols are the same as in the left plot. Bottom left: emission spectroscopy metric (ESM) vs. planet mass. Bottom right: ESM vs. planet T_{eq}. TIC 46432937 b has the highest value of TSM or ESM for a transiting warm super-Jupiter with $M_p > 3.0\,M_J$ and $T_{eq} < 1000$ K.

TIC 46432937 b. The next highest TSM value for a planet with $M_p > 3.0\,M_J$ and $T_{eq} < 1000$ K is 13.1 for the planet HAT-P-20 b (G. Á. Bakos et al. 2011), which is a factor of 4 smaller than the value for TIC 46432937 b. TIC 46432937 b also has a high value of ESM for a giant planet with $T_{eq} < 1000$ K. The only giant planet that has $T_{eq} < 1000$ K and a higher ESM value than TIC 46432937 b is WASP-80 b (A. H. M. J. Triaud et al. 2013), with ESM = 216. WASP-80 b also has a significantly lower mass of $0.538 \pm 0.035\,M_J$. Thus TIC 46432937 b presents a particularly good opportunity for studying the atmosphere of a warm, high-mass planet. The frequent transits of this $P = 1.4404$ days system should also facilitate scheduling such observations.

Table 8
Adopted Limb-darkening Coefficients for TOI 762 A b and TIC 46432937 b

Parameter	TOI 762 A b Value	TIC 46432937 b Value
c_1, g	0.65 ± 0.14	⋯
c_2, g	0.09 ± 0.16	⋯
c_1, r	0.44 ± 0.14	⋯
c_2, r	0.30 ± 0.17	⋯
c_1, i	0.23 ± 0.12	⋯
c_2, i	0.13 ± 0.15	⋯
c_1, zs	0.13 ± 0.11	⋯
c_2, zs	0.10 ± 0.12	⋯
c_1, $I+z$	0.37 ± 0.15	⋯
c_2, $I+z$	$0.28^{+0.14}_{-0.19}$	⋯
c_1, Z	⋯	0.143 ± 0.096
c_2, Z	⋯	0.15 ± 0.14
c_1, Y	⋯	$0.108^{+0.097}_{-0.071}$
c_2, Y	⋯	0.06 ± 0.12
c_1, J	⋯	0.142 ± 0.088
c_2, J	⋯	0.09 ± 0.13
c_1, H	⋯	0.20 ± 0.11
c_2, H	⋯	0.08 ± 0.15
c_1, z–H	$0.050^{+0.066}_{-0.037}$	⋯
c_2, z–H	-0.000 ± 0.071	⋯
c_1, T	0.132 ± 0.091	0.20 ± 0.10
c_2, T	0.02 ± 0.13	0.17 ± 0.14

Note. For all systems we adopt a model in which the orbit is assumed to be circular. See the discussion in Section 3.3. The values listed are for a quadratic law. The limb-darkening parameters were directly varied in the fit, using the tabulations from A. Claret et al. (2012, 2013) and A. Claret (2018) to place Gaussian prior constraints on their values, assuming a prior uncertainty of 0.2 for each coefficient.

Acknowledgments

We thank the anonymous referee for their careful reading this paper, and helpful comments that have improved the quality of the work. J.H. and G.B. acknowledge funding from NASA grant No. 80NSSC22K0315. A.J. and R.B. acknowledge support from ANID—Millennium Science Initiative—ICN12_009. R.B. acknowledges support from FONDECYT Project 11200751. A.J. acknowledges support from FONDECYT project 1210718. We acknowledge funding from the European Research Council under the ERC Grant Agreement No. 337591-ExTrA. This research has made use of the Exoplanet Follow-up Observation Program (ExoFOP; DOI:10.26134/ExoFOP5) website, which is operated by the California Institute of Technology, under contract with the National Aeronautics and Space Administration under the Exoplanet Exploration Program. This paper made use of data collected by the TESS mission and which are publicly available from the Mikulski Archive for Space Telescopes (MAST) operated by the Space Telescope Science Institute (STScI). Funding for the TESS mission is provided by NASA's Science Mission Directorate. The specific observations from MAST analyzed in this paper can be accessed from DOI:10.17909/e3cp-9907. We acknowledge the use of public TESS data from pipelines at the TESS Science Office and at the TESS Science Processing Operations Center. Resources supporting this work were provided by the NASA High-End Computing (HEC) Program through the NASA Advanced Supercomputing (NAS) Division at Ames Research Center for the production of the SPOC data products. This research has made use of the NASA Exoplanet Archive, which is operated by the California Institute of Technology, under contract with the National Aeronautics and Space Administration under the Exoplanet Exploration Program. The contributions at the Mullard Space Science Laboratory by EMB have been supported by STFC through the consolidated grant ST/W001136/1. The postdoctoral fellowship of K.B. is funded by F.R.S.-FNRS grant T.0109.20 and by the Francqui Foundation. This publication benefits from the support of the French Community of Belgium in the context of the FRIA Doctoral Grant awarded to M.T. M.G. is F.R.S.-FNRS Research Director and E.J. is F.R.S.-FNRS Senior Research Associate. F.J. P. acknowledges financial support from the grant CEX2021-001131-S funded by MCIN/AEI/ 10.13039/501100011033 and through projects PID2019-109522GB-C52 and PID2022-137241NB-C43. Based on data collected by the SPECULOOS-South Observatory at the ESO Paranal Observatory in Chile. The ULiege's contribution to SPECULOOS has received funding from the European Research Council under the European Union's Seventh Framework Programme (FP/2007-2013; grant Agreement No. 336480/SPECULOOS), from the Balzan Prize and Francqui Foundations, from the Belgian Scientific Research Foundation (F.R.S.-FNRS; grant No. T.0109.20), from the University of Liege, and from the ARC grant for Concerted Research Actions financed by the Wallonia-Brussels Federation. This work is supported by a grant from the Simons Foundation (PI: Queloz; grant No. 327127). Based on data collected by the TRAPPIST-South telescope at the ESO La Silla Observatory. TRAPPIST is funded by the Belgian Fund for Scientific Research (Fond National de la Recherche Scientifique, FNRS) under the grant No. PDR T.0120.21, with the participation of the Swiss National Science Fundation (SNF). D.R. was supported by NASA under award number NNA16BD14C for NASA Academic Mission Services.

Facilities: TESS, LCOGT, TRAPPIST, Gaia, ExTrA, SPECULOOS, VLT:ESPRESSO, Exoplanet Archive, IRSA, ZTF, ASAS-SN.

Software: VARTOOLS (J. D. Hartman & G. Á. Bakos 2016), MWDUST (J. Bovy et al. 2016), Astropy (Astropy Collaboration et al. 2013, 2018), ESPRESSO DRS pipeline v2.3.5 (D. Sosnowska et al. 2015; A. Modigliani et al. 2020), EsoReflex (W. Freudling et al. 2013), AstroImageJ (K. A. Collins et al. 2017).

ORCID iDs

Joel D. Hartman https://orcid.org/0000-0001-8732-6166
Daniel Bayliss https://orcid.org/0000-0001-6023-1335
Rafael Brahm https://orcid.org/0000-0002-9158-7315
Edward M. Bryant https://orcid.org/0000-0001-7904-4441
Andrés Jordán https://orcid.org/0000-0002-5389-3944
Gáspár Á. Bakos https://orcid.org/0000-0001-7204-6727
Melissa J. Hobson https://orcid.org/0000-0002-5945-7975
Elyar Sedaghati https://orcid.org/0000-0002-7444-5315
Xavier Bonfils https://orcid.org/0000-0001-9003-8894
Jose Manuel Almenara https://orcid.org/0000-0003-3208-9815
Khalid Barkaoui https://orcid.org/0000-0003-1464-9276
Mathilde Timmermans https://orcid.org/0009-0008-2214-5039
Elsa Ducrot https://orcid.org/0000-0002-7008-6888
Sebastián Zúñiga-Fernández https://orcid.org/0000-0002-9350-830X
Matthew J. Hooton https://orcid.org/0000-0003-0030-332X
Peter Pihlmann Pedersen https://orcid.org/0000-0002-5220-609X
Francisco J. Pozuelos https://orcid.org/0000-0003-1572-7707

Amaury H. M. J. Triaud https://orcid.org/0000-0002-5510-8751
Michaël Gillon https://orcid.org/0000-0003-1462-7739
Emmanuel Jehin https://orcid.org/0000-0001-8923-488X
William C. Waalkes https://orcid.org/0000-0002-8961-0352
Zachory K. Berta-Thompson https://orcid.org/0000-0002-3321-4924
Steve B. Howell https://orcid.org/0000-0002-2532-2853
Elise Furlan https://orcid.org/0000-0001-9800-6248
George R. Ricker https://orcid.org/0000-0003-2058-6662
Roland Vanderspek https://orcid.org/0000-0001-6763-6562
Sara Seager https://orcid.org/0000-0002-6892-6948
Joshua N. Winn https://orcid.org/0000-0002-4265-047X
Jon M. Jenkins https://orcid.org/0000-0002-4715-9460
David Rapetti https://orcid.org/0000-0003-2196-6675
Karen A. Collins https://orcid.org/0000-0001-6588-9574
David Charbonneau https://orcid.org/0000-0002-9003-484X
Christopher J. Burke https://orcid.org/0000-0002-7754-9486
David R. Rodriguez https://orcid.org/0000-0003-1286-5231

References

Addison, B. C., Knudstrup, E., Wong, I., et al. 2021, AJ, 162, 292
Almenara, J. M., Bonfils, X., Bryant, E. M., et al. 2024, A&A, 683, A166
Antoniadis-Karnavas, A., Sousa, S. G., Delgado-Mena, E., et al. 2020, A&A, 636, A9
Artigau, É., Hébrard, G., Cadieux, C., et al. 2021, AJ, 162, 144
Astropy Collaboration, Price-Whelan, A. M., Sipőcz, B. M., et al. 2018, AJ, 156, 123
Astropy Collaboration, Robitaille, T. P., Tollerud, E. J., et al. 2013, A&A, 558, A33
Bakos, G. Á., Bayliss, D., Bento, J., et al. 2020, AJ, 159, 267
Bakos, G. Á., Hartman, J., Torres, G., et al. 2011, ApJ, 742, 116
Bakos, G. Á., Torres, G., Pál, A., et al. 2010, ApJ, 710, 1724
Barkaoui, K., Burdanov, A., Hellier, C., et al. 2019, AJ, 157, 43
Bayliss, D., Gillen, E., Eigmüller, P., et al. 2018, MNRAS, 475, 4467
Bensby, T., Feltzing, S., & Oey, M. S. 2014, A&A, 562, A71
Bento, J., Schmidt, B., Hartman, J. D., et al. 2017, MNRAS, 468, 835
Bonfils, X., Almenara, J. M., Jocou, L., et al. 2015, Proc. SPIE, 9605, 96051L
Borucki, W. J., Koch, D., Basri, G., et al. 2010, Sci, 327, 977
Bovy, J., Rix, H.-W., Green, G. M., Schlafly, E. F., & Finkbeiner, D. P. 2016, ApJ, 818, 130
Brown, T. M., Baliber, N., Bianco, F. B., et al. 2013, PASP, 125, 1031
Bryant, E. M., Bayliss, D., & Van Eylen, V. 2023, MNRAS, 521, 3663
Burdanov, A. Y., de Wit, J., Gillon, M., et al. 2022, PASP, 134, 105001
Caldwell, D. A., Tenenbaum, P., Twicken, J. D., et al. 2020, RNAAS, 4, 201
Cañas, C. I., Kanodia, S., Bender, C. F., et al. 2022, AJ, 164, 50
Cañas, C. I., Kanodia, S., Libby-Roberts, J., et al. 2023, AJ, 166, 30
Cañas, C. I., Stefansson, G., Kanodia, S., et al. 2020, AJ, 160, 147
Choi, J., Dotter, A., Conroy, C., et al. 2016, ApJ, 823, 102
Claret, A. 2018, A&A, 618, A20
Claret, A., Hauschildt, P. H., & Witte, S. 2012, A&A, 546, A14
Claret, A., Hauschildt, P. H., & Witte, S. 2013, A&A, 552, A16
Cointepas, M., Almenara, J. M., Bonfils, X., et al. 2021, A&A, 650, A145
Collins, K. 2019, AAS Meeting Abstracts, 233, 140.05
Collins, K. A., Kielkopf, J. F., Stassun, K. G., & Hessman, F. V. 2017, AJ, 153, 77
Cutri, R. M., Wright, E. L., Conrow, T., et al. 2021, yCat, II/328
Delamer, M., Kanodia, S., Cañas, C. I., et al. 2024, ApJL, 962, L22
Delrez, L., Gillon, M., Queloz, D., et al. 2018, Proc. SPIE, 10700, 107001I
Dorval, P., Talens, G. J. J., Otten, G. P. P. L., et al. 2020, A&A, 635, A60
Dotter, A. 2016, ApJS, 222, 8
El-Badry, K., Rix, H.-W., & Heintz, T. M. 2021, MNRAS, 506, 2269
Foreman-Mackey, D., Hogg, D. W., Lang, D., & Goodman, J. 2013, PASP, 125, 306
Freudling, W., Romaniello, M., Bramich, D. M., et al. 2013, A&A, 559, A96
Gaia Collaboration, Vallenari, A., Brown, A. G. A., et al. 2023, A&A, 674, A1
Gan, T., Cadieux, C., Jahandar, F., et al. 2023, AJ, 166, 165
Gan, T., Lin, Z., Wang, S. X., et al. 2022, MNRAS, 511, 83
Garcia, L. J., Timmermans, M., Pozuelos, F. J., et al. 2021, prose: FITS images processing pipeline, Astrophysics Source Code Library, ascl:2111.006
Garcia, L. J., Timmermans, M., Pozuelos, F. J., et al. 2022, MNRAS, 509, 4817
Gillon, M., Jehin, E., Magain, P., et al. 2011, EPJ Web of Conferences, 11, 06002
Guerrero, N. M., Seager, S., Huang, C. X., et al. 2021, ApJS, 254, 39
Hamann, A., Montet, B. T., Fabrycky, D. C., Agol, E., & Kruse, E. 2019, AJ, 158, 133
Hansen, B. M. S., & Barman, T. 2007, ApJ, 671, 861
Hart, K., Shappee, B. J., Hey, D., et al. 2023, arXiv:2304.03791
Hartman, J. D., & Bakos, G. Á. 2016, A&C, 17, 1
Hartman, J. D., Bakos, G. Á., Bayliss, D., et al. 2019, AJ, 157, 55
Hartman, J. D., Bakos, G. Á., Csubry, Z., et al. 2023, AJ, 166, 163
Hartman, J. D., Bayliss, D., Brahm, R., et al. 2015, AJ, 149, 166
Hartman, J. D., Jordán, A., Bayliss, D., et al. 2020, AJ, 159, 173
Hartman, Z. D., & Lépine, S. 2020, ApJS, 247, 66
Hobson, M. J., Jordán, A., Bryant, E. M., et al. 2023, ApJL, 946, L4
Howell, S. B., Everett, M. E., Sherry, W., Horch, E., & Ciardi, D. R. 2011, AJ, 142, 19
Huang, C. X., Vanderburg, A., Pál, A., et al. 2020a, RNAAS, 4, 204
Huang, C. X., Vanderburg, A., Pál, A., et al. 2020b, RNAAS, 4, 206
Jehin, E., Gillon, M., Queloz, D., et al. 2011, Msngr, 145, 2
Jenkins, J. M. 2002, ApJ, 575, 493
Jenkins, J. M., Caldwell, D. A., Chandrasekaran, H., et al. 2010, ApJL, 713, L87
Jenkins, J. M., Tenenbaum, P., Seader, S., et al. 2020, Kepler Data Processing Handbook: Transiting Planet Search (Washington, DC: NASA), https://archive.stsci.edu/files/live/sites/mast/files/home/missions-and-data/kepler/_documents/KSCI-19081-002-KDPH.pdf
Jenkins, J. M., Twicken, J. D., McCauliff, S., et al. 2016, Proc. SPIE, 9913, 99133E
Jensen, E. 2013, Tapir: A Web Interface for Transit/Eclipse Observability, Astrophysics Source Code Library, ascl:1306.007
Johnson, J. A., Gazak, J. Z., Apps, K., et al. 2012, AJ, 143, 111
Jordán, A., Hartman, J. D., Bayliss, D., et al. 2022, AJ, 163, 125
Kagetani, T., Narita, N., Kimura, T., et al. 2023, PASJ, 75, 713
Kanodia, S., Libby-Roberts, J., Cañas, C. I., et al. 2022, AJ, 164, 81
Kanodia, S., Mahadevan, S., Libby-Roberts, J., et al. 2023, AJ, 165, 120
Kanodia, S., Stefansson, G., Cañas, C. I., et al. 2021, AJ, 162, 135
Kempton, E. M. R., Bean, J. L., Louie, D. R., et al. 2018, PASP, 130, 114401
Kiseleva, L. G., Eggleton, P. P., & Mikkola, S. 1998, MNRAS, 300, 292
Kovács, G., Zucker, S., & Mazeh, T. 2002, A&A, 391, 369
Kozai, Y. 1962, AJ, 67, 591
Kreidberg, L. 2015, PASP, 127, 1161
Kunimoto, M., Daylan, T., Guerrero, N., et al. 2022, ApJS, 259, 33
Leconte, J., Chabrier, G., Baraffe, I., & Levrard, B. 2010, A&A, 516, A64
Li, J., Tenenbaum, P., Twicken, J. D., et al. 2019, PASP, 131, 024506
Li, S. L., Agnor, C. B., & Lin, D. N. C. 2010, ApJ, 720, 1161
Lidov, M. L. 1962, P&SS, 9, 719
Lillo-Box, J., Figueira, P., Leleu, A., et al. 2020, A&A, 642, A121
Lin, D. N. C., Bodenheimer, P., & Richardson, D. C. 1996, Natur, 380, 606
Liu, S.-F., Agnor, C. B., Lin, D. N. C., & Li, S.-L. 2015, MNRAS, 446, 1685
Mandel, K., & Agol, E. 2002, ApJL, 580, L171
Masci, F. J., Laher, R. R., Rusholme, B., et al. 2019, PASP, 131, 018003
McQuillan, A., Mazeh, T., & Aigrain, S. 2014, ApJS, 211, 24
Modigliani, A., Freudling, W., Anderson, R. I., et al. 2020, in ASP Conf. Ser. 527, Astronomical Data Analysis Software and Systems XXIX, ed. R. Pizzo et al. (San Francisco, CA: ASP), 667
Murray, C. A., Delrez, L., Pedersen, P. P., et al. 2020, MNRAS, 495, 2446
Naoz, S. 2016, ARA&A, 54, 441
NASA Exoplanet Archive 2024, Planetary Systems Table, IPAC, doi:10.26133/NEA12
Ngo, H., Knutson, H. A., Hinkley, S., et al. 2016, ApJ, 827, 8
Nielsen, L. D., Brahm, R., Bouchy, F., et al. 2020, A&A, 639, A76
Paxton, B., Bildsten, L., Dotter, A., et al. 2011, ApJS, 192, 3
Paxton, B., Cantiello, M., Arras, P., et al. 2013, ApJS, 208, 4
Paxton, B., Marchant, P., Schwab, J., et al. 2015, ApJS, 220, 15
Pepe, F., Cristiani, S., Rebolo, R., et al. 2021, A&A, 645, A96
Popinchalk, M., Faherty, J. K., Kiman, R., et al. 2021, ApJ, 916, 77
Ribas, I., Font-Ribera, A., & Beaulieu, J.-P. 2008, ApJL, 677, L59
Ricker, G. R., Winn, J. N., Vanderspek, R., et al. 2015, JATIS, 1, 014003
Riello, M., De Angeli, F., Evans, D. W., et al. 2021, A&A, 649, A3
Schönrich, R., Binney, J., & Dehnen, W. 2010, MNRAS, 403, 1829
Scott, N. J., Howell, S. B., Gnilka, C. L., et al. 2021, FrASS, 8, 138
Sebastian, D., Gillon, M., Ducrot, E., et al. 2021, A&A, 645, A100
Shappee, B. J., Prieto, J. L., Grupe, D., et al. 2014, ApJ, 788, 48
Skrutskie, M. F., Cutri, R. M., Stiening, R., et al. 2006, AJ, 131, 1163

Smith, J. C., Stumpe, M. C., Van Cleve, J. E., et al. 2012, PASP, 124, 1000
Sosnowska, D., Lovis, C., Figueira, P., et al. 2015, in ASP Conf. Ser. 495, Astronomical Data Analysis Software an Systems XXIV (ADASS XXIV), ed. A. R. Taylor & E. Rosolowsky (San Francisco, CA: ASP), 285
Stumpe, M. C., Smith, J. C., Catanzarite, J. H., et al. 2014, PASP, 126, 100
Stumpe, M. C., Smith, J. C., Van Cleve, J. E., et al. 2012, PASP, 124, 985
Susemiehl, N., & Meyer, M. R. 2022, A&A, 657, A48
Tayar, J., Claytor, Z. R., Huber, D., & van Saders, J. 2022, ApJ, 927, 31
Torres, G., Konacki, M., Sasselov, D. D., & Jha, S. 2004, ApJ, 614, 979
Triaud, A. H. M. J., Anderson, D. R., Collier Cameron, A., et al. 2013, A&A, 551, A80
Triaud, A. H. M. J., Dransfield, G., Kagetani, T., et al. 2023, MNRAS, 525, L98
Twicken, J. D., Catanzarite, J. H., Clarke, B. D., et al. 2018, PASP, 130, 064502
Zacharias, N., Finch, C. T., Girard, T. M., et al. 2013, AJ, 145, 44
Zechmeister, M., & Kürster, M. 2009, A&A, 496, 577
Zhou, G., Huang, C. X., Bakos, G. Á., et al. 2019, AJ, 158, 141